

## A GCSS model intercomparison for a tropical squall line observed during TOGA–COARE. I: Cloud-resolving models

By J.-L. REDELSPERGER<sup>1</sup>\* P. R. A. BROWN<sup>2</sup>, F. GUICHARD<sup>1</sup>, C. HOFF<sup>1</sup>, M. KAWASIMA<sup>3</sup>, S. LANG<sup>4</sup>, T. MONTMERLE<sup>5</sup>, K. NAKAMURA<sup>6</sup>, K. SAITO<sup>7</sup>, C. SEMAN<sup>8</sup>, W. K. TAO<sup>4</sup> and L. J. DONNER<sup>8</sup>

<sup>1</sup>*Centre National de Recherche Météorologiques, France*

<sup>2</sup>*Joint Centre for Mesoscale Meteorology, UK*

<sup>3</sup>*Institute of Low Temperature Science, Japan*

<sup>4</sup>*Goddard Space Flight Center, USA*

<sup>5</sup>*Centre d'étude des Environnements Terrestre et Planétaires, France*

<sup>6</sup>*Ocean Research Institute, Japan*

<sup>7</sup>*Meteorology Research Institute, Japan*

<sup>8</sup>*Geophysical Fluid Dynamics Laboratory, USA*

(Received 27 July 1998, revised 14 April 1999)

### SUMMARY

Results from eight cloud-resolving models are compared for the first time for the case of an oceanic tropical squall line observed during the Tropical Ocean/Global Atmosphere Coupled Ocean–Atmosphere Response Experiment. There is broad agreement between all the models in describing the overall structure and propagation of the squall line and some quantitative agreement in the evolution of rainfall. There is also a more qualitative agreement between the models in describing the vertical structure of the apparent heat and moisture sources.

The three-dimensional (3D) experiments with an active ice phase and open lateral boundary conditions along the direction of the system propagation show good agreement for all parameters. The comparison of 3D simulated fields with those obtained from two different analyses of airborne Doppler radar data indicates that the 3D models are able to simulate the dynamical structure of the squall line, including the observed double-peaked updraughts. However, the second updraught peak at around 10 km in height is obtained only when the ice phase is represented. The 2D simulations with an ice-phase parametrization also exhibit this structure, although with a larger temporal variability.

In the 3D simulations, the evolution of the mean wind profile is in the sense of decreasing the shear, but the 2D simulations are unable to reproduce this behaviour.

**KEYWORDS:** Cloud-resolving models Clouds Doppler radar GCSS

### INTRODUCTION

Current general-circulation models (GCMs) use sophisticated parametrizations to represent the effects of clouds and precipitation and their interactions with other physical processes occurring in the atmosphere. To evaluate and improve these parametrizations, it is important to compare them with observations and more detailed numerical models. In response to this challenge, the GEWEX<sup>†</sup> Cloud Systems Study (GCSS) has established a strategy based on the use of cloud-resolving models (CRMs), single-column models (SCMs) and observations.

The Precipitating Convective Cloud Systems Group of the GCSS has recently initiated two projects designed firstly to evaluate CRMs against observational datasets, and secondly to evaluate SCMs against numerical datasets produced by CRMs (Moncrieff *et al.* 1997). In the last decade, the numerical modelling of convective systems has shown that CRMs are an effective means of simulating many of their observed features; this is especially true for squall-line systems. Nevertheless, no detailed intercomparison of CRMs for a precipitating convective case has been successfully accomplished, in contrast with the many intercomparisons of GCMs (e.g. Gates 1992; Slingo *et al.* 1996) and boundary-layer models (e.g. Moeng *et al.* 1996; Bretherton *et al.* 1999) that

\* Corresponding author: CNRM/GAME, CNRS and Météo-France, 42 Av Coriolis, 31057 Toulouse Cedex, France.

<sup>†</sup> Global Energy and Water-cycle EXperiment.

have been conducted. One of the tasks of the Precipitating Convective Cloud Systems Group is to fill this gap, and this is also the main object of the present paper. Previous intercomparisons of boundary-layer large-eddy simulations (LES) have highlighted differences between the models resulting from differences in the physical parametrizations used within the CRMs (e.g. Moeng *et al.* 1996). These include, particularly, the representation of microphysics and radiation. Similar sensitivities of models can be expected for simulations of deep convective systems. Two projects, both based on the Tropical Ocean/Global Atmosphere Coupled Ocean–Atmosphere Response Experiment (TOGA–COARE), have been designed with two different approaches.

The first topic of study of the GCSS is the detailed study of a squall line on a time-scale of hours. It is an initial-value problem in which the simulated convective system is to be evaluated in a deterministic fashion. Squall lines can be considered as self-forced convection (e.g. Tao *et al.* 1997), creating by themselves large-scale tendencies of heat, moisture and momentum. For this reason, no external forcing tendencies are imposed. To simulate such convective systems, CRMs generally use open lateral boundary conditions along the propagation direction (e.g. Redelsperger and Lafore 1988).

The second GCSS topic concerns the multi-day evolution of cloud systems in response to large-scale forcing, and seeks a statistical realization of the cloud system (Krueger 1998). The large-scale tendencies are derived from observations and are imposed on the CRMs using periodic lateral boundary conditions. The mean wind is also continuously nudged towards the observed mean values. This approach is sometimes referred to as ‘cloud ensemble modelling’.

The present paper concerns the first topic. It corresponds to an oceanic squall-line system observed during the TOGA–COARE by the two NOAA P3 aircraft (Jorgensen *et al.* 1997). Squall lines belong to a broad class of precipitating systems that are commonly observed in mid-latitude and tropical regions (e.g. Houze 1977; Rutledge *et al.* 1988; Chong *et al.* 1987). During the TOGA–COARE, squall lines were often observed (LeMone *et al.* 1998); Rickenbach and Rutledge (1998) found that almost two-thirds of the precipitating systems observed by shipboard radar during the four-month intensive observing period corresponded to the class of large-scale linearly structured systems to which squall lines belong. Squall lines are characterized by fast propagation, by dramatic changes of thermodynamical and dynamical parameters in the direction perpendicular to them and, in many cases, by the development of a stratiform precipitation region behind the convective leading edge. These characteristics lead to fundamental issues for the representation of squall lines in GCMs. These include the large effective sources of heat, moisture and momentum, the different vertical distributions of these sources in the convective and stratiform regions, the mass transports between convective and stratiform regions and the initiation of such systems.

This paper describes a study of experiments performed by eight different CRMs and the comparison of their results against observational data for the squall line. It includes an evaluation of the impact of parametrizations used in the CRMs as well as numerical features such as the dimensionality of the model grid (i.e. two-dimensional (2D) versus three-dimensional (3D) model grids) and the choice of lateral boundary conditions, issues best addressed on a case-study basis. This case also provides the framework in which to test a new method for the forcing of SCMs using information derived from CRMs (Redelsperger *et al.* 1996). This latter work is reported in a companion paper (Bechtold *et al.* 2000). Data from airborne Doppler radar, yielding 3D fields of wind and reflectivity, are used to determine to what extent CRMs are able to reproduce the main structure of the observed cloud system.

TABLE LIST OF MODELS THAT PARTICIPATED IN THIS STUDY

Research group	Research scientists	Model acronym	Model references
	T. Montmerle		Lafore <i>et al.</i> (1998) Pinty and Jabouille (1993)
CNRM	F. Guichard J.-L. Redelsperger	COME-NH	Redelsperger and Sommeria (1986) Caniaux <i>et al.</i> (1994)
	S. Lang W.-K. Tao	GCE	Tao and Simpson (1993)
	C. Seman L. Donner	LAN	Donner <i>et al.</i> (1999) Held <i>et al.</i> (1993)
	M. Kawashima		Lin <i>et al.</i> (1983)
JCMM	P. Brown		Shutts and Gray (1994) Swann (1996)
	K. Saito	MRI-NHM	Ikawa and Saito (1991) Saito and Kato (1996)
ORI	K. Nakamura	ARPS	Xue <i>et al.</i> (1995)

The acronyms in the first column are defined as follows:

CETP—Centre d'étude des Environnements Terrestre et Planétaires, France;

CNRM—Centre National de Recherches Météorologiques, France;

GSFC—Goddard Space Flight Center, USA;

GFDL—Geophysical Fluid Dynamics Laboratory, USA;

ILTS—Institute of Low Temperature Science, Japan;

JCMM—Joint Centre for Mesoscale Meteorology, UK;

MRI—Meteorology Research Institute, Japan;

ORI—Ocean Research Institute, Japan.

## 2 DESCRIPTION OF CRMS

The eight different models that have been used in this intercomparison project are listed in Table 1, together with their sources of documentation. These models are hereafter referred to by the group acronyms given in the first column of this table. Brief descriptions of the eight models are given in Table 2. All the models were developed independently using different equation systems and were run in either 2D or 3D configurations, except for the CNRM model which was run in both 2D and 3D. The different dynamical formulations were of minor importance in the present study, but the dimensionality of the models can lead to some quantitative differences. Two other factors capable of leading to differences in results are the choice of lateral boundary conditions and the treatment of microphysics. Two types of lateral boundary conditions have been used: periodic and open (Table 2). Open lateral boundary conditions were recommended to be used along the propagation direction of the squall line, as it is well known that large differences in the thermodynamics and wind profiles exist between the inflow and outflow regions (e.g. Zipser 1977). Nevertheless, some models were not designed to allow such sophisticated lateral boundary conditions. In order to avoid the problem of spurious interactions between the inflow and outflow regions of the simulated squall line, 2D models using periodic lateral boundary conditions were run within a 1000 km horizontal domain; the diagnostics were computed only over a sub-domain of 100 km in order to be comparable with CRMs run over 100 km domains with open lateral boundary conditions. The GFDL 3D model was run over a

TABLE 2. KEY CHARACTERISTICS OF THE CLOUD-RESOLVING MODELS USED IN THE INTERCOMPARISON

Research group	Dynamical system	Model dimensions	Latitudinal boundary conditions	Subgrid-scale closure	Water cycle (number of classes)
	A	3D	Open		No ice (2) Ice (5)
CNRM	A	3D 2D	Open	.5 order	No ice (2) Ice (5)
GSFC	C-S	3D	Open ( <i>x</i> -axis) Periodic ( <i>y</i> -axis)	.5 order	Ice (5)
GFDL	C	3D	Periodic	order	Ice (4)
	A	2D	Open	order	Ice (5)
	A	2D	Periodic	order	Ice (5)
	C	2D	Open	.5 order	No ice (2) Ice (5)
ORI	C-S	2D	Open	.5 order	No ice (2)

The following notation is used in column 2:

A—anelastic;

C-I—elastic with implicit sound waves;

C-S—elastic with time splitting.

small domain with periodic lateral boundary conditions in both horizontal directions (Table 2), allowing the assessment of differences induced by the choice of lateral boundary conditions. Simulations of precipitating convective systems with trailing stratiform regions are expected to be sensitive to the representation of the microphysics (e.g. Yoshizaki 1986; Nicholls 1987; Chen and Cotton 1988; Tao and Simpson 1989; Caniaux *et al.* 1995; Liu *et al.* 1997). In the present case, the models were run with different microphysical parametrizations both with and without an ice phase. The parametrizations represented between two and five different classes of particles (Table 2), including cloud droplets, rain drops, ice crystals, aggregates, and graupel. A detailed description of each of the eight models is not possible in the present paper but references are given in Table 1.

### 3. CASE DESCRIPTION AND NUMERICAL EXPERIMENTS

#### (a) Case description and initial conditions

The general approach of this first intercomparison was to choose a case sufficiently simple to be capable of being simulated by several different models. On the other hand, the selected case needed to include sufficient physical features to be able to be compared with Doppler radar observations and to be useful in the evaluation of GCM convection and cloud parametrizations.

The selected case was a 100 kilometre-long squall line observed during the TOGA-COARE on 22 February 1993. It was well sampled by airborne Doppler radar (Fig. 1) as it approached Honiara island. The two NOAA P-3 aircraft flew for over five hours to sample the system. This case has been also chosen as a test case for intercomparisons of different radar retrieval techniques. The convective system has been extensively studied using both observations and CRMs by several other groups (Jorgensen *et al.* 1997;

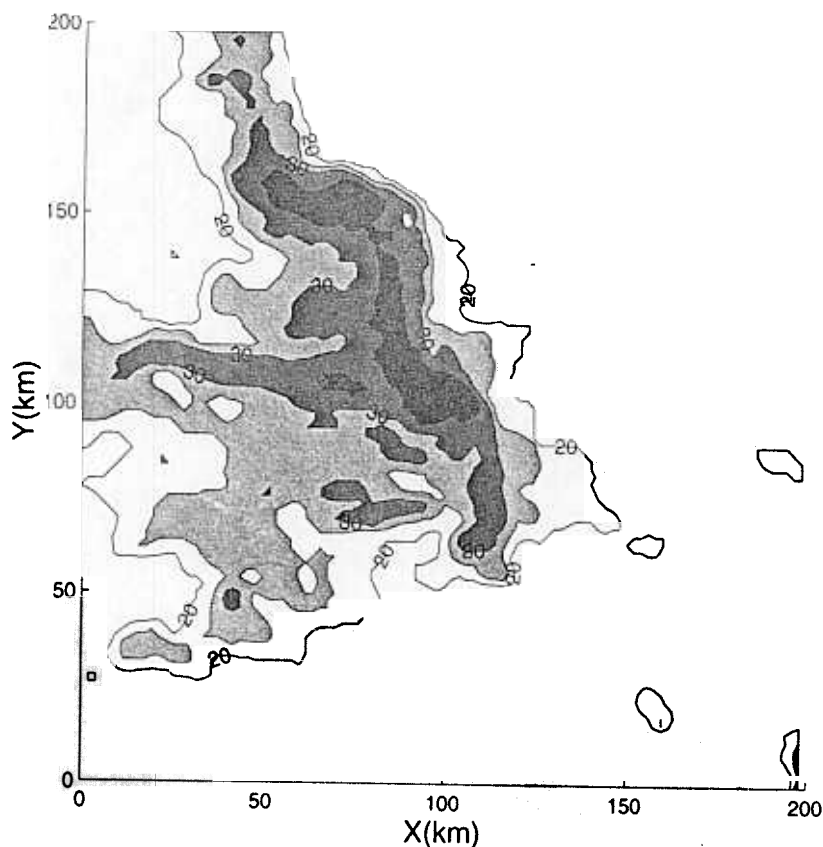


Figure 1 Horizontal cross-section of airborne radar reflectivity (dBZ) at 2215 UTC 22 February 1993 at a height of 500 m over a domain of 200 km  $\times$  200 km.

Trier *et al.* 1996, 1997; Wang *et al.* 1996; Montmerle and Lemaitre 1998). The near-environment has been characterized by LeMone *et al.* (1994) in the form of a composite sounding derived from both rawinsonde observations (Honiara site) and P-3 aircraft data. The convective available potential energy (CAPE) for irreversible pseudoadiabatic ascent of an air parcel averaged through the lowest 50 hPa is around  $1500 \text{ J kg}^{-1}$ . The sounding is characterized by moderate instability and a very moist environment (relative humidity around 90% between 0 and 5 km). These thermodynamical conditions are thought to be representative of the environment of many tropical oceanic convective systems. The composite hodograph valid at 0600 local time (Fig. 2) indicates the presence of a low-level jet (with a speed of about  $12 \text{ m s}^{-1}$ ) at 2 km above ground level. The squall line was observed to be oriented nearly perpendicular to the low-level shear vector, travelling at a speed of  $12 \text{ m s}^{-1}$ . At low levels, a drop of 15 K in the equivalent potential temperature was observed across the leading edge.

For the present numerical experiments, the sounding data (geopotential height  $Z$ , pressure  $P$ , potential temperature  $\theta$ , specific humidity  $Q$ , and horizontal wind components  $U$  and  $V$ ) were specified on a stretched vertical grid with 35 m resolution at the lowest level increasing to 750 m in the upper troposphere (Table 3). The use of such a stretched vertical grid was strongly recommended since, for example, the observed height of the cold pool was lower than 600 m. The recommended domain size for the 3D simulations was 21 km high (using the stretched vertical grid that is given in Table 3—all the models used this vertical grid spacing) by 100 km along the  $x$ -axis (west–east) and 125 km along the  $y$ -axis (south–north) with a horizontal grid spacing of 1250 m. The actual horizontal domains used by the various models are shown in

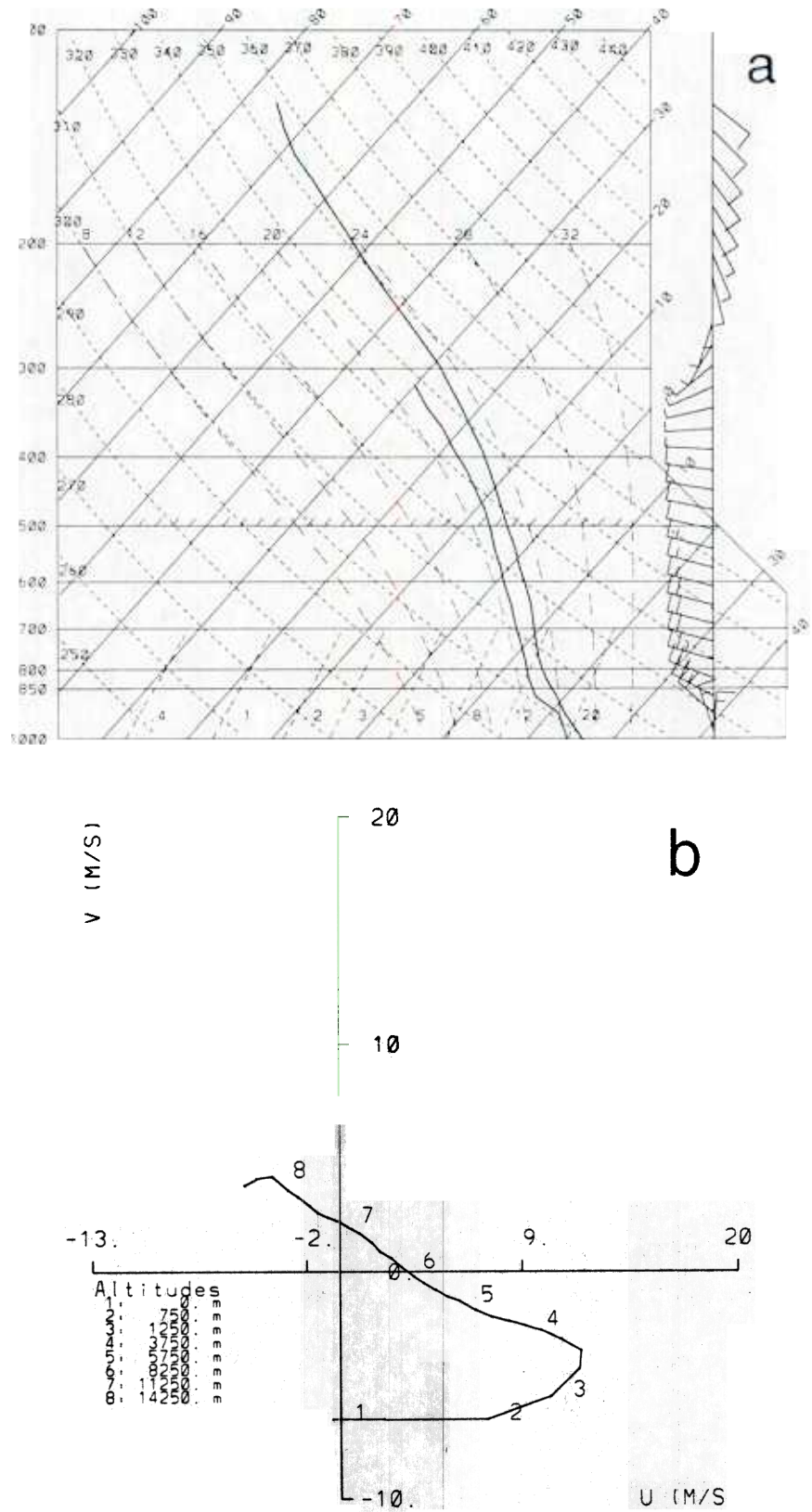


Figure 2. Specified initial conditions for the model runs. (a) Temperature and specific humidity plotted on a skew- $T$  log- $P$  diagram and (b) the horizontal wind components ( $U$  positive towards the east and  $V$  positive towards the north) plotted on a hodograph—data courtesy of M. A. LeMone.

TABLE 3. THE INITIAL SOUNDING USED BY THE MODELS

	$U$ ( $\text{m s}^{-1}$ )	$V$ ( $\text{m s}^{-1}$ )	$\theta$ (K)	$Q$ ( $\text{g g}^{-1}$ )	$P$ (Pa)
35.5	-0.03	-6.50	299.413	$0.199 \times 10^{-1}$	100202.7
110.3	0.75	-6.50	299.653	$0.196 \times 10^{-1}$	99363.9
192.9	1.61	-6.50	299.917	$0.193 \times 10^{-1}$	98439.7
285.7	2.57	-6.50	300.214	$0.190 \times 10^{-1}$	97412.9
391.4	3.67	-6.50	300.552	$0.186 \times 10^{-1}$	96268.3
512.2	4.93	-6.50	300.939	$0.182 \times 10^{-1}$	94959.8
650.2	6.36	-6.50	301.381	$0.177 \times 10^{-1}$	93464.5
807.4	7.77	-6.39	301.941	$0.169 \times 10^{-1}$	91789.1
985.5	8.91	-6.03	302.689	$0.156 \times 10^{-1}$	89945.3
1186.1	10.19	-5.63	303.531	$0.142 \times 10^{-1}$	87869.3
1410.4	11.05	-5.12	304.377	$0.132 \times 10^{-1}$	85622.1
1659.7	11.75	-4.52	305.275	$0.125 \times 10^{-1}$	83158.5
1934.8	12.04	-4.00	306.450	$0.118 \times 10^{-1}$	80524.1
2236.6	12.10	-3.52	307.839	$0.111 \times 10^{-1}$	77680.3
2565.7	11.47	-3.18	309.668	$0.104 \times 10^{-1}$	74724.6
2922.4	10.76	-2.86	311.700	$0.962 \times 10^{-2}$	71604.6
3306.9	10.01	-2.58	313.941	$0.880 \times 10^{-2}$	68354.7
3719.2	9.35	-2.41	316.415	$0.806 \times 10^{-2}$	65020.9
4159.1	8.65	-2.24	318.727	$0.718 \times 10^{-2}$	61630.5
4626.2	7.82	-2.05	321.081	$0.640 \times 10^{-2}$	58188.1
5120.0	7.01	-1.78	323.772	$0.561 \times 10^{-2}$	54723.0
5639.7	6.18	-1.39	326.370	$0.489 \times 10^{-2}$	51262.2
6184.2	5.48	-1.13	329.158	$0.419 \times 10^{-2}$	47829.4
6752.5	4.80	-0.80	332.113	$0.340 \times 10^{-2}$	44448.8
7343.3	4.11	-0.44	335.148	$0.269 \times 10^{-2}$	41166.0
7954.8	3.45	-0.04	337.919	$0.202 \times 10^{-2}$	37975.3
8585.5	2.76	0.47	340.509	$0.145 \times 10^{-2}$	34889.2
9233.4	2.02	0.89	343.037	$0.101 \times 10^{-2}$	31920.6
9896.4	1.42	1.42	345.351	$0.641 \times 10^{-3}$	29113.7
10572.2	0.74	1.83	346.909	$0.403 \times 10^{-3}$	26444.8
11258.2	-0.01	2.20	348.215	$0.228 \times 10^{-3}$	23917.0
11951.8	-0.80	2.48	349.504	$0.477 \times 10^{-4}$	21569.9
12650.1	-1.42	2.84	350.900	$0.100 \times 10^{-4}$	19373.1
13400.1	-2.25	3.39	352.040	$0.100 \times 10^{-5}$	17209.5
14150.1	-3.24	4.08	352.680	$0.100 \times 10^{-5}$	15226.0
14900.1	-3.24	4.08	354.960	$0.100 \times 10^{-5}$	13421.1
15650.1	-3.24	4.08	358.180	$0.100 \times 10^{-5}$	11783.7
16400.1	-3.24	4.08	363.341	$0.100 \times 10^{-5}$	10312.2
17150.1	-3.24	4.08	377.021	$0.100 \times 10^{-5}$	9006.9
17900.1	-3.24	4.08	386.421	$0.100 \times 10^{-5}$	7860.9
18650.1	-3.24	4.08	400.521	$0.100 \times 10^{-5}$	6850.3
19400.1	-3.24	4.08	414.621	$0.100 \times 10^{-5}$	5968.3
20150.1	-3.24	4.08	428.721	$0.100 \times 10^{-5}$	5194.1
20900.1	-3.24	4.08	442.821	$0.100 \times 10^{-5}$	4517.6

Table 4. To keep the convective system inside the simulation domain, a constant system velocity was specified ( $12 \text{ m s}^{-1}$  along the  $x$ -axis and  $-2 \text{ m s}^{-1}$  along the  $y$ -axis). Some simulations were run with surface fluxes computed from fixed surface conditions of  $P_{\text{surface}} = 1006 \text{ hPa}$ ,  $T_{\text{surface}} = 301.3 \text{ K}$  and  $Q_{\text{surface}} = 23.2 \text{ g kg}^{-1}$ .

Even if squall lines are able to create their own forcing, their initiation remains an issue from both observational and modelling perspectives. In order to be able to compare the control and sensitivity experiments, we chose to use the same initiation set-up. The

TABLE 4. CRM EXPERIMENTS PERFORMED

Experiment acronym	Figure label	Research group	Ice phase	Surface fluxes	Radiation	$L_x$ (km)	$L_y$ (km)	Lateral boundary condition
	RSI	GFDL	Ice	Yes	Yes	100	125	Periodic
		CNRM	Ice	Yes	Yes	100	125	Open
		GSFC	Ice	Yes	Yes	360 <sup>#</sup>	160 <sup>#</sup>	Open-periodic
RSI2D	RSI	JCMM	Ice	Yes	Yes <sup>†</sup>	1000*		Periodic
		CNRM	Ice	Yes	Yes	100		Open
SI2D	SI	CNRM	Ice	Yes	No	100		
RI2D	RI	JCMM	Ice	No	Yes <sup>†</sup>	1000*		Periodic
ICE3D	I	CETP	Ice	No	No	100	125	
		CNRM	Ice	No	No	100	125	
ICE2D		JCMM	Ice	No	No	1000*		Periodic
		MRI	Ice	No	No	100		Open
		CNRM	Ice	No	No	100		Open
		ILTS	Ice	No	No	1000*		Open
CONT3D	C	CETP	No Ice	No	No	100	125	Open
		CNRM	No Ice	No	No	100	125	Open
CONT2D	C	MRI	No Ice	No	No	100		Open
		ORI	No Ice	No	No	1000*		Open
		JCMM	No Ice	No	No	1000*		Periodic
		CNRM	No Ice	No	No	100		Open

\* Diagnostics have been computed on the central part (100 km) of the two-dimensional domain.

<sup>#</sup> Diagnostics have been computed on the central part (100 × 125 km) of the three-dimensional domain.

<sup>†</sup> Long-wave radiation only.

convection was initiated by a line of four low-level cold pools gradually introduced through specified cooling and drying rates. These cooling and drying rates were turned off after the first 20 minutes of simulation. The cold pools were vertically uniform and applied in the first 2.5 km of the domain. Their horizontal shape and amplitude are given by the following equations:

$$\left(\frac{\partial\theta}{\partial t}\right)_i = 6.7 \times 10^{-3} \cos^2\left(\frac{\pi d}{2}\right) \text{ K s}^{-1} \quad (1)$$

$$\left(\frac{\partial q}{\partial t}\right)_i = .675 \times 10^{-6} \cos^2\left(\frac{\pi d}{2}\right) \text{ g g}^{-1} \text{ s}^{-1} \quad (2)$$

where  $d = \sqrt{\{(x - x_c)/x_r\}^2 + \{(y - y_c)/y_r\}^2}$ . If  $d > 1.0$ ,  $(\partial\theta/\partial t)_i = (\partial q/\partial t)_i = 0$ .

The semi-axes of the elliptical cold pools,  $x_r$  and  $y_r$ , are 7 and 6 km, respectively.  $x - x_c$  and  $y - y_c$  are the relative distances from the centre of each cold pool, located at 15 km intervals in the  $y$ -direction. This initiation by cooling and drying is an artifice used to lead rapidly to a sustainable squall line in the simulations. The density current produced by the cold pool collapse is, however, expected to be representative of that associated with the observed convective system.

In addition to the recommended 3D simulations, 2D simulations with the same resolution and  $x$ - $z$  domain were also performed. The intercomparison of the 2D and 3D simulations was an important issue for the project. Indeed, in order to allow multi-day simulations with CRMs and to conduct additional sensitivity tests, it is important to

know the degree of confidence that one can have in 2D simulations. The 2D assumption is justified to the extent that the variations of thermodynamical and dynamical quantities in squall lines are larger in the line-normal direction than in the line-parallel one.

The choice of top boundary conditions was left to each modeller. Since the domain size in the 3D models was similar to the scale of convective systems, open lateral boundary conditions, which allow the development of circulations at scales larger than the convective system, are more realistic than periodic lateral boundary conditions. Also, open lateral boundary conditions allow the advection of hydrometeors produced by the squall line, and the application of different environmental conditions in front of and behind the convective system. The use of a large domain along the propagation direction avoids these issues but, for practical reasons, this is only feasible in 2D (See Table 4). Two of the 3D integrations examined the impact of using periodic boundary conditions: GFDL (periodic in both  $x$  and  $y$ ) and GSFC (open in  $x$  but periodic in  $y$ ). For reasons given above, differences between these models and those 3D models using open lateral boundary conditions in both directions (CNRM and CETP) can be expected to be larger with the GFDL model than with the GSFC model.

### (b) Model experiments and diagnoses

Table 4 gives a summary of the numerical experiments performed in the present intercomparison. 2D and 3D simulations were made with eight different CRMs. Sensitivity tests on microphysical parametrizations, surface fluxes, radiation, domain size and dimensionality (i.e. 2D or 3D) have been conducted.

An agreed list of diagnostic data necessary for intercomparing the models was established, together with methods for their computation from the simulations (Redelsperger *et al.* 1996). These included:

(i) time series of maximum and minimum vertical velocity, convective and stratiform surface rain rate, domain average of cloud amount, vapour content, cloud water content, rain water content, total ice content, surface fluxes, upward and downward short-wave radiative flux, and upward and downward long-wave radiative flux;

(ii) vertical profiles of the horizontal average of  $u$ ,  $v$ ,  $w$ , density, potential temperature, water vapour mixing ratio, cloud water content, rain water content, total solid water content, short-wave and long-wave radiative fluxes, apparent heat and moisture sources and sinks, apparent  $u$ -momentum and  $v$ -momentum sources, radiative sources, diabatic heating and mass fluxes.

Computation of these profiles was requested for different parts of the domain, namely the convective updraught and downdraught regions, the stratiform region and the cloud-free region. Vertical and horizontal cross-sections were also requested. Formats for the exchange of all these data were specified in a manner that kept them as simple as possible to allow numerous, fast and easy, exchanges between participants.

In order to compare the effects of the squall line on the atmosphere, i.e. the apparent sources of heat, moisture and momentum due to the convective system and its component parts, it is necessary to define them in the framework of the CRM. The forcing for the heat sources and moisture sinks are defined as:

$$\left(\frac{\partial \theta}{\partial t}\right)_{\text{frc}} = \frac{1}{\bar{\rho}} \frac{\partial \bar{\rho} \bar{w} \bar{\theta}}{\partial z} - \frac{\partial \bar{u} \bar{\theta}}{\partial x} - \frac{\partial \bar{v} \bar{\theta}}{\partial y}, \quad (3)$$

$$\left(\frac{\partial q_v}{\partial t}\right)_{\text{frc}} = \frac{1}{\bar{\rho}} \frac{\partial \bar{\rho} \bar{w} \bar{q}_v}{\partial z} - \frac{\partial \bar{u} \bar{q}_v}{\partial x} - \frac{\partial \bar{v} \bar{q}_v}{\partial y} \quad (4)$$

where  $\theta$  is the potential temperature,  $q_v$  the mixing ratio of water vapour, and  $\rho$  the density. The overbar denotes a horizontal average of the variable over the domain and a time average over 1 hour. The apparent heat source  $Q_{1C}$  and moisture sink  $Q_2$  for the total domain are then defined as:

$$\begin{aligned} \overline{Q_{1C}} &\equiv \overline{Q_1} - \overline{Q_R} - \pi \left\{ \frac{\partial \theta}{\partial t} - \left( \frac{\partial \theta}{\partial t} \right)_{\text{frc}} \right\} \overline{Q_R} \\ \overline{Q_2} &= -\frac{L}{c} \overline{\frac{\partial q_v}{\partial t} - \left( \frac{\partial q_v}{\partial t} \right)_{\text{frc}}} \end{aligned} \quad (6)$$

where  $\pi = (T/\theta) = (p/p_0)^{R/C_p}$  and  $Q_R$  is the radiative term.

There is no general agreement about the best way to separate stratiform and convective columns. The present study uses a method similar to that of Tao *et al.* (1993). A cloudy grid box is defined as one in which the mixing ratio for total hydrometeors exceeds  $5 \times 10^{-6} \text{ g g}^{-1}$ . A first simple criterion for the convective/stratiform separation is that any vertical column with a surface rain rate  $\geq 20 \text{ mm h}^{-1}$  is considered as convective. In addition, vertical columns for which the surface rain rate exceeds  $\geq 4 \text{ mm h}^{-1}$  and is twice as large as the average taken over the 24 surrounding grid points in the 3D models (4 in the 2D models) are identified as the cores of convective cells. For each such core column, the 8 surrounding columns in 3D (2 in 2D) are also considered as convective columns. Cloudy columns not classified as convective are considered to be stratiform.

Similarly, it is possible to define an apparent momentum source, representing the effects of unresolved convective circulations on the mesoscale momentum field. The large-scale forcing for  $u$ - and  $v$ -momentum is defined as:

$$\left( \frac{\partial \rho u}{\partial t} \right)_{\text{frc}} = -\frac{\partial \bar{\rho} \bar{w} \bar{u}}{\partial z} - \bar{\rho} \frac{\partial \bar{u} \bar{u}}{\partial x} - \bar{\rho} \frac{\partial \bar{u} \bar{v}}{\partial y} - \frac{\partial \bar{P}}{\partial x} \quad (7)$$

$$\left( \frac{\partial \rho v}{\partial t} \right)_{\text{frc}} = -\frac{\partial \bar{\rho} \bar{w} \bar{v}}{\partial z} - \bar{\rho} \frac{\partial \bar{u} \bar{v}}{\partial x} - \bar{\rho} \frac{\partial \bar{v} \bar{v}}{\partial y} - \frac{\partial \bar{P}}{\partial y} \quad (8)$$

The apparent sources of  $u$ -momentum and  $v$ -momentum are then defined as:

$$\begin{aligned} \overline{Q_u} &= \left\{ \overline{\frac{\partial \rho u}{\partial t}} - \left( \frac{\partial \rho u}{\partial t} \right)_{\text{frc}} \right\} \\ \overline{Q_v} &= \left\{ \overline{\frac{\partial \rho v}{\partial t}} - \left( \frac{\partial \rho v}{\partial t} \right)_{\text{frc}} \right\} \end{aligned} \quad (9)$$

The eight SCMs have also been run with the same initial conditions and with imposed large-scale tendencies of temperature and moisture (Eqs. (3) and (4)) deduced from experiments with an open-boundary CRM (Redelsperger *et al.* 1996). Results from these SCMs are reported in a companion paper (Bechtold *et al.* 1999).

It is worth noting that the forcing terms specified by Eqs. (3), (4), (7) and (8) are identically zero for CRMs running with periodic lateral boundary conditions when computed on the full simulation domain. Indeed, the horizontal average of  $w$  over the domain is equal to zero in this case, as well the horizontal average of horizontal gradients. Consequently, when it was possible, and as noted in Table 4, the computations of these quantities were made over a sub-domain of a size identical to that of the recommended domain in the intercomparison (i.e. 100 km in the  $x$ -direction).

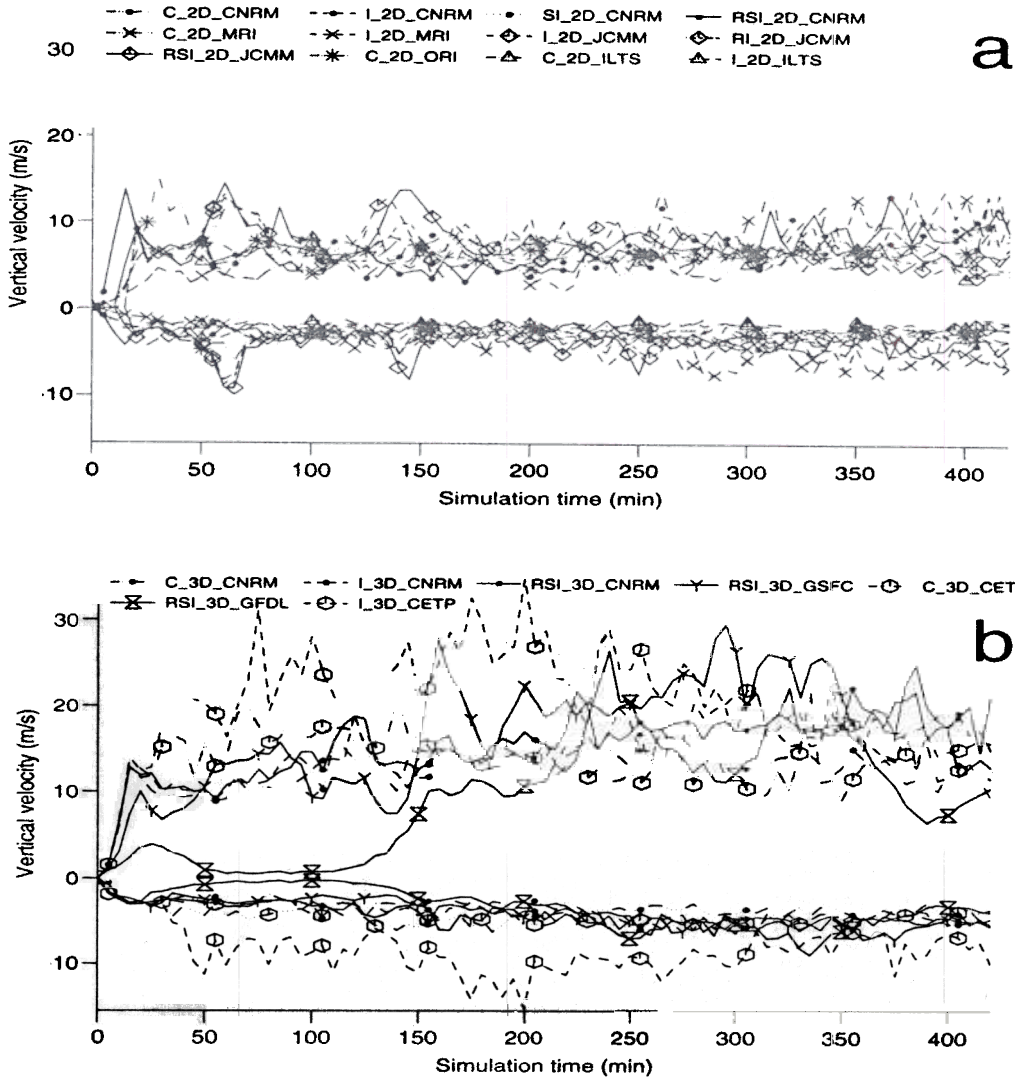


Figure 3. Time history of the maximum and minimum vertical velocity ( $m s^{-1}$ ) for (a) the 2D cloud-resolving models, and (b) the 3D cloud-resolving models (see Tables 1 and 4 for an explanation of the acronyms).

#### 4. RESULTS

Overall, both 2D and 3D models were able to simulate a number of qualitative features of the squall line. These include a leading convective region with large precipitation rate, a stratiform region of reduced precipitation rates, a large system propagation speed and a warming and drying of the atmosphere. The comparison of some fields did, however, show significant quantitative differences. In this paper, it is possible to present only a small amount of data gathered during the intercomparison project. The interested reader can also find a comprehensive collection of the results on the WWW page dedicated to this case (URL: <http://www.cnrm.meteo.fr/gcss/>).

##### (a) Time series

Figure 3 shows the time history of the maximum and minimum vertical velocities for the 2D and 3D simulations. Each class of experiments generates a family of curves with general agreement between all models. The spin-up time of the convection for the triggering used is roughly the same for each model except GFDL. The 3D experiments

exhibit generally more variations between them than the 2D experiments. The 2D experiments produce significantly smaller values (half the magnitude) compared with the 3D experiments. For both the 2D and the 3D experiments, the downdraught values are approximately half the updraught ones, a result also true for the mean values in the convective region. The total surface rain rate (Fig. 4) exhibits larger differences from experiment to experiment for an individual model, and from model to model for the same experiment. Nevertheless, independently of the type of experiment, the results stay in the same general range of values apart from the GFDL 3D model using periodic lateral boundary conditions in both horizontal directions. The lower precipitation rates, but similar vertical velocity extrema, of the GFDL model during the later part of the simulation suggest that it has a reduced area fraction of convective cells in comparison with the other 3D models. The 2D results are generally close to those of the 3D models except for the two first hours.

It is important to note that in the present simulations, the models are not constrained by an imposed large-scale forcing. We are looking at an initial value problem where the simulated convective systems formed their own large-scale forcing. Fast-propagating squall lines are considered to be self-forced systems creating their own convergence zones and large-scale ascent. The main input from large scales for such systems is the convective available potential energy. Keeping in mind these considerations and looking at 3D results for the total surface rain (Fig. 4), there is quite good agreement between simulations using ice-phase microphysics and open lateral boundary conditions along the direction of system propagation (CNRM, CETP and GSFC). The inclusion of an ice parametrization results in a small increase in precipitation for both 2D and 3D experiments. Experiments taking into account surface fluxes and/or radiative processes lead to a slight increase in precipitation. Another feature also apparent in the time evolution of the rainfall (Fig. 4), is that the 2D experiments show more temporal variations on scales of 20–100 min than the 3D experiments. Surface rain rates were further partitioned into stratiform and convective parts, which are important to know for SCMs (see Bechtold *et al.* 1999). The time history of the stratiform rain rate (Fig. 5) again shows general agreement between the 3D models except for the GFDL model. On average 70% of the total rain rate is convective and 30% stratiform. This partitioning was found by shipborne radar to be common for systems observed during disturbed periods of the TOGA-COARE (Short *et al.* 1997).

From both Figs. 4(c) and 5(c), it is clear that the main problem in the GFDL simulation stems from an insufficiently developed stratiform region. One possible reason is the use of a small domain (100 km) with periodic lateral boundary conditions in both horizontal directions. In contrast, the GSFC 3D model with periodic lateral boundary conditions in only one direction produces similar stratiform precipitation and slightly less convective precipitation than the other 3D models with fully open boundary conditions (CNRM and CETP). Opening the boundary conditions in the propagation direction has, therefore, a large impact. In the GFDL simulation with full periodic lateral boundary conditions, non-zero domain-averaged vertical motions cannot develop. Since the domain size in this simulation is not much larger than the system itself, this precludes the development of a larger-scale circulation which can intensify the convective system through positive feedback. This behaviour differs from the 3D simulations with open boundary conditions in the propagation direction (CNRM, CETP and GSFC), which develop domain-averaged vertical motions, as discussed later. The domain-averaged vertical motions in the latter simulations, with their vertical velocity peaks in the middle and upper troposphere, generate convective instability. In addition the use of periodic lateral boundary conditions along the propagation direction on a small domain imposes

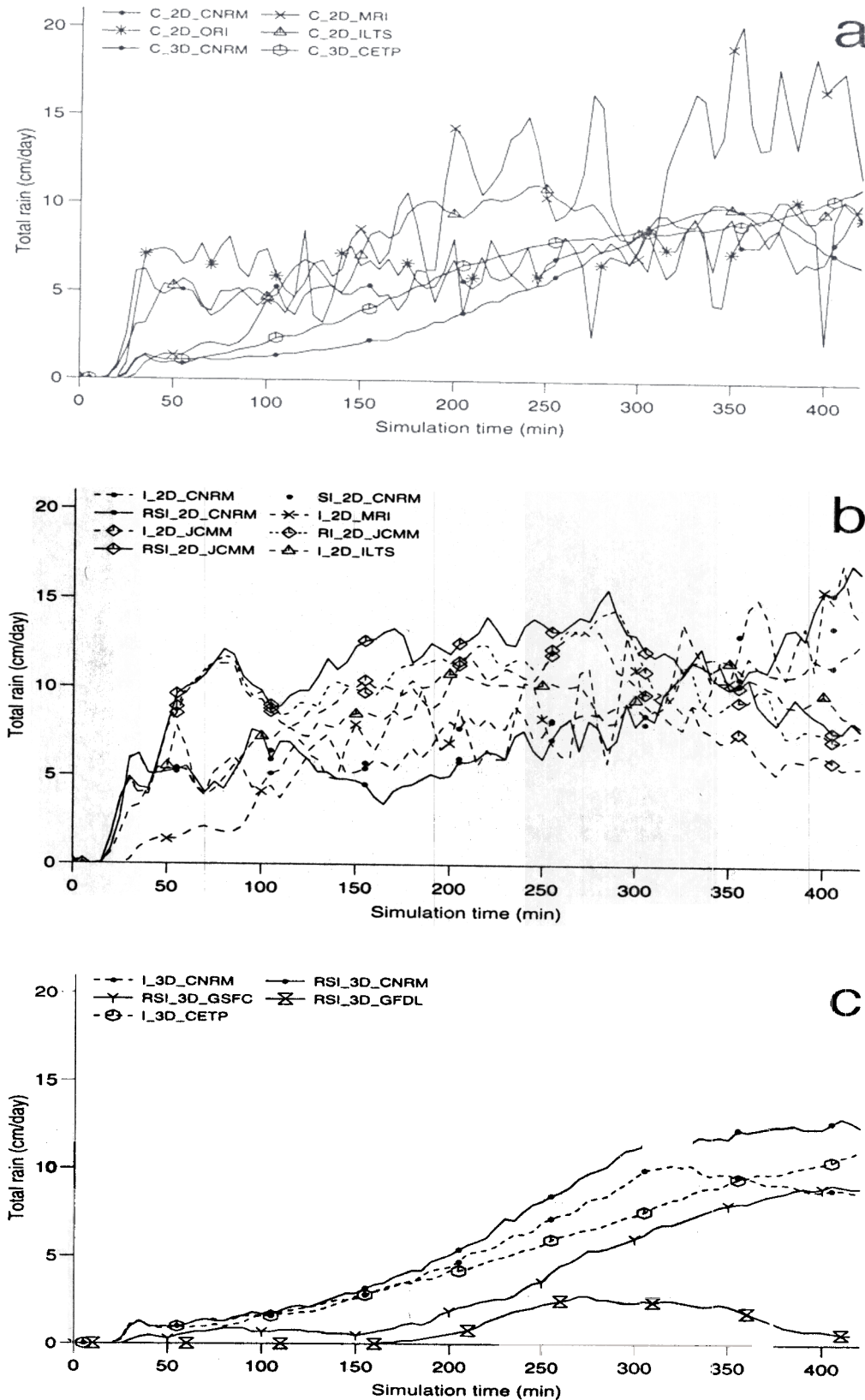


Figure 4. Time history of the total surface rain rate ( $\text{cm day}^{-1}$ ) for (a) the 2D and 3D cloud-resolving models (CRMs) with no ice-phase parametrization, (b) the 2D CRMs with an ice-phase parametrization, and (c) the 3D CRMs with an ice-phase parametrization (see Tables 1 and 4 for an explanation of the acronyms).

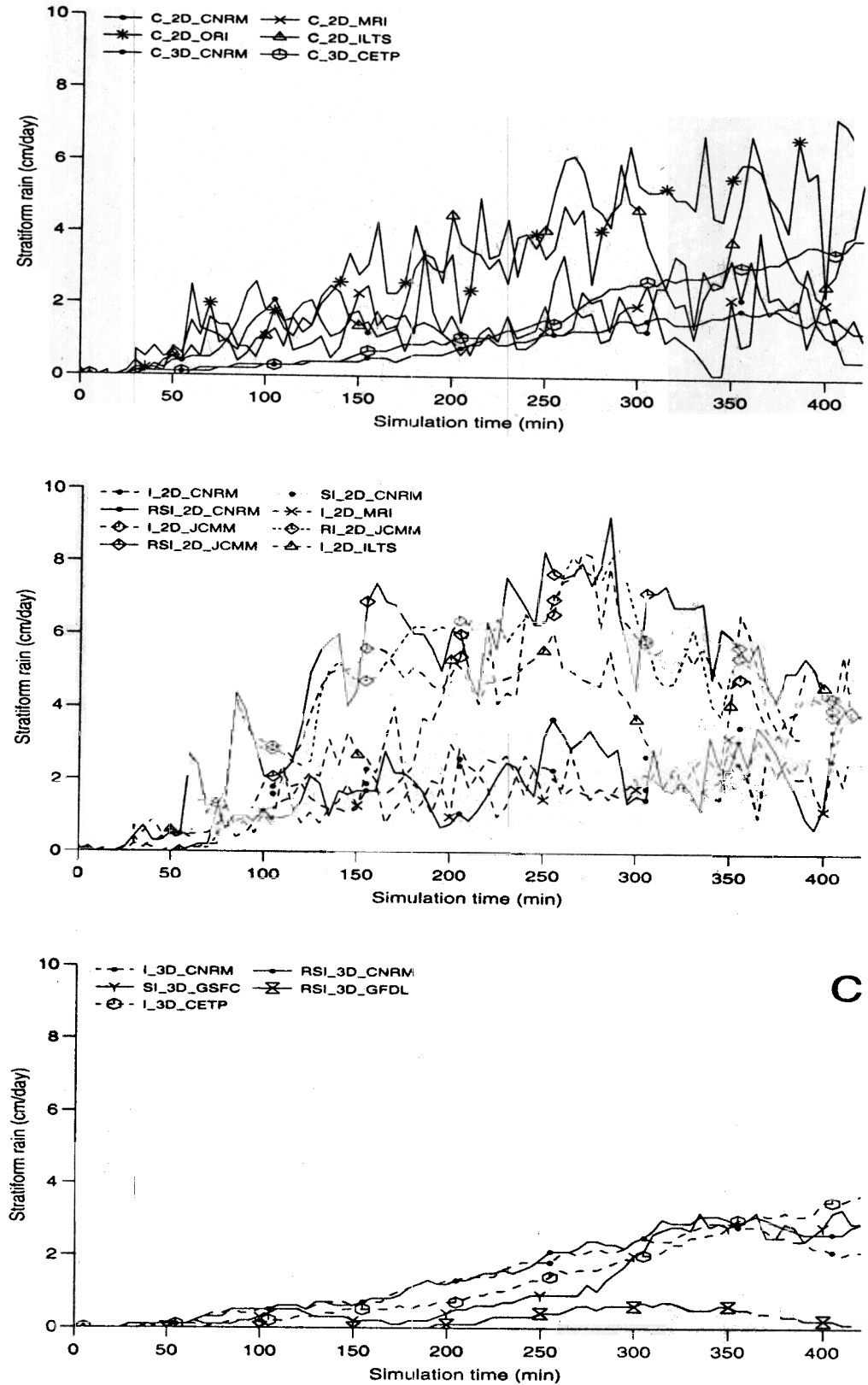


Figure 5. As Fig. 4, but for the stratiform surface rain rate ( $\text{cm day}^{-1}$ ).

the same atmospheric characteristics both in front of and behind the convective system. Thus, the 3D convective system with periodic lateral boundary conditions generates considerably less precipitation. Figures 4(c) and 5(c) imply that precipitation from both the convective and the stratiform regions in the GFDL simulation is less than in the other 3D simulations. With less generation of convective instability possible in this simulation, the convective circulations are less developed. There is, in turn, less condensate available to feed the stratiform component of the system.

Confirming these points, the JCMM experiments using a large 2D domain (1000 km) together with periodic lateral boundary conditions are able to produce large stratiform regions. In the 2D experiments, differences in the partitioning between convective and stratiform regions come from differences in the microphysical schemes. For example, lower terminal fall speeds of ice hydrometeors generally correspond to a reduced stratiform region as they allow for the hydrometeors formed in the convective region to be advected farther to the rear of the system. As seen in Fig. 5(b), the JCMM 2D model with an ice phase produces larger amounts of stratiform rainfall than other models. Further tests with this model have shown that this discrepancy is reduced when the mean fall-speed of cloud ice is increased.

Comparisons of the time evolution of domain-averaged liquid and solid (when present) water content (Fig. 6) indicate a generally good agreement, except (and for the same reasons as above) for the GFDL experiment with periodic lateral boundary conditions, and for the three 2D experiments produced from the JCMM model. Again, tests with the JCMM model have shown that this discrepancy is reduced when the mean fall-speed of cloud ice is increased. Apart from these differences, the agreement is quite noticeable and encouraging. In particular, it is important to note that the 2D and 3D models have similar quantitative behaviours. Also, the ice phase does not seem to be important for predicting the domain-averaged total water content. This is to be expected since the 4 km depth between cloud base and the freezing level means that much of the rain will be formed by coalescence/collection even in those models with an ice phase, and experiments without an ice phase can produce liquid water above the 0°C isotherm level. Of course, we should still expect differences in the vertical distributions of the hydrometeors.

### (b) *Three-dimensional structure*

Examination of horizontal cross-sections of the simulations at different times indicates that the 3D experiments are able to reproduce to some extent the different stages of the observed system as it develops from the linear-configuration stage to the bow-shaped stage (Fig. 7). As observed by airborne radar (Fig. 1), the convective region formed at the leading edge of the system which was moving to the east (on the right in the figures), corresponding to strong convective updraughts and downdraughts (Fig. 8). Behind the convective region, an extended stratiform region is simulated with less intense vertical motions and lower water contents. More detailed comparisons show that the 3D models are also able to simulate the observed mesoscale horizontal vortices occurring on the northern and southern parts of the system (Trier *et al.* 1997; Montmerle *et al.* (personal communication)). Nevertheless, the comparison of horizontal cross-sections shows that there are some qualitative and quantitative differences between experiments after 6 h of simulation. Again, the use of periodic lateral boundary conditions on a relatively small domain (GFDL) decreases the intensity of the system and leads to a less developed stratiform region (Figs. 7(b) and 8(b)). On the other hand, the values of vertical velocity and total water content agree quite well for the three other experiments (CETP, CNRM and GSFC). As confirmed by the time series of vertical velocity extrema (Fig. 3), the

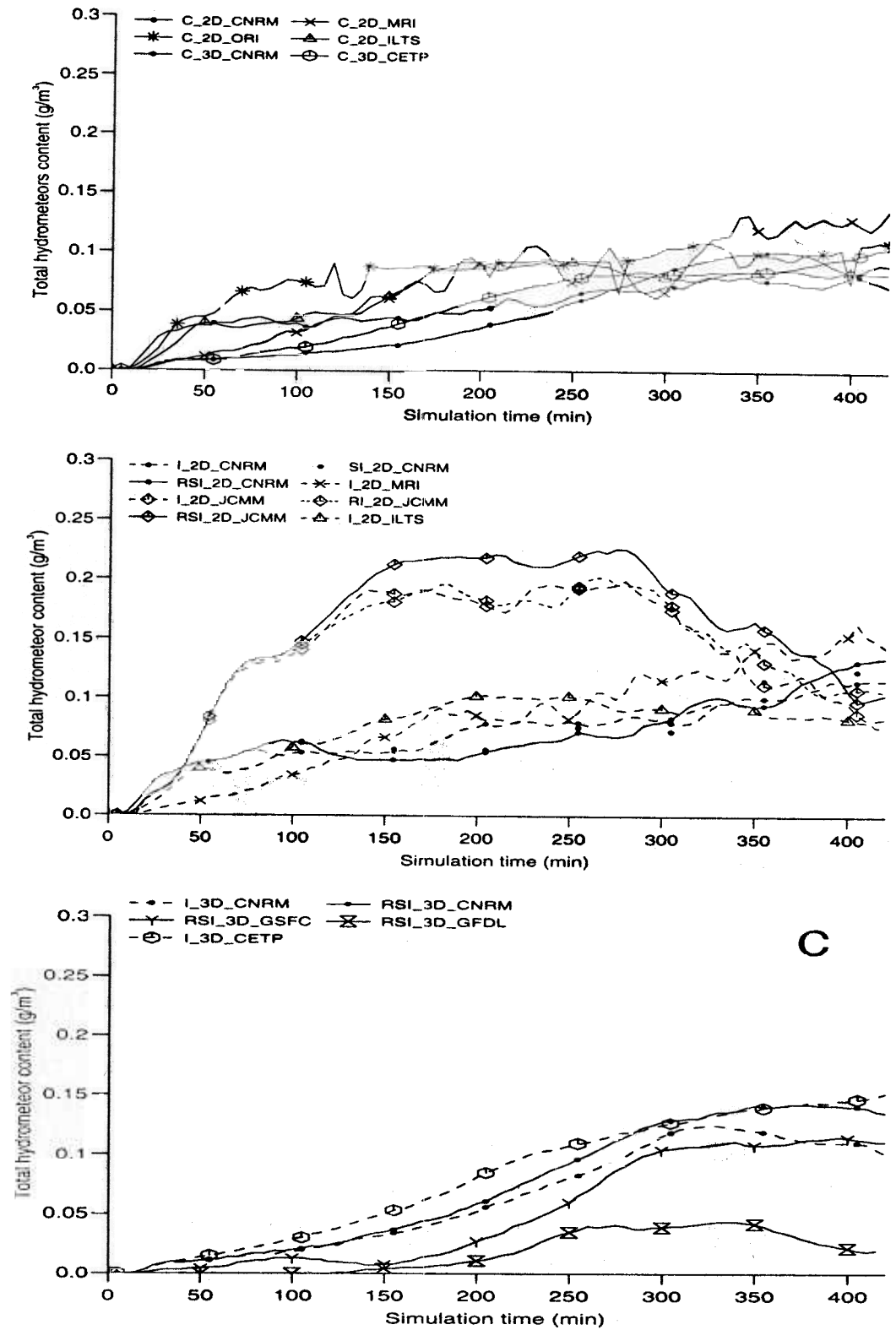


Figure 6. As Fig. 4, but for the domain-averaged total hydrometeor (liquid + solid) water content ( $\text{g m}^{-3}$ ).

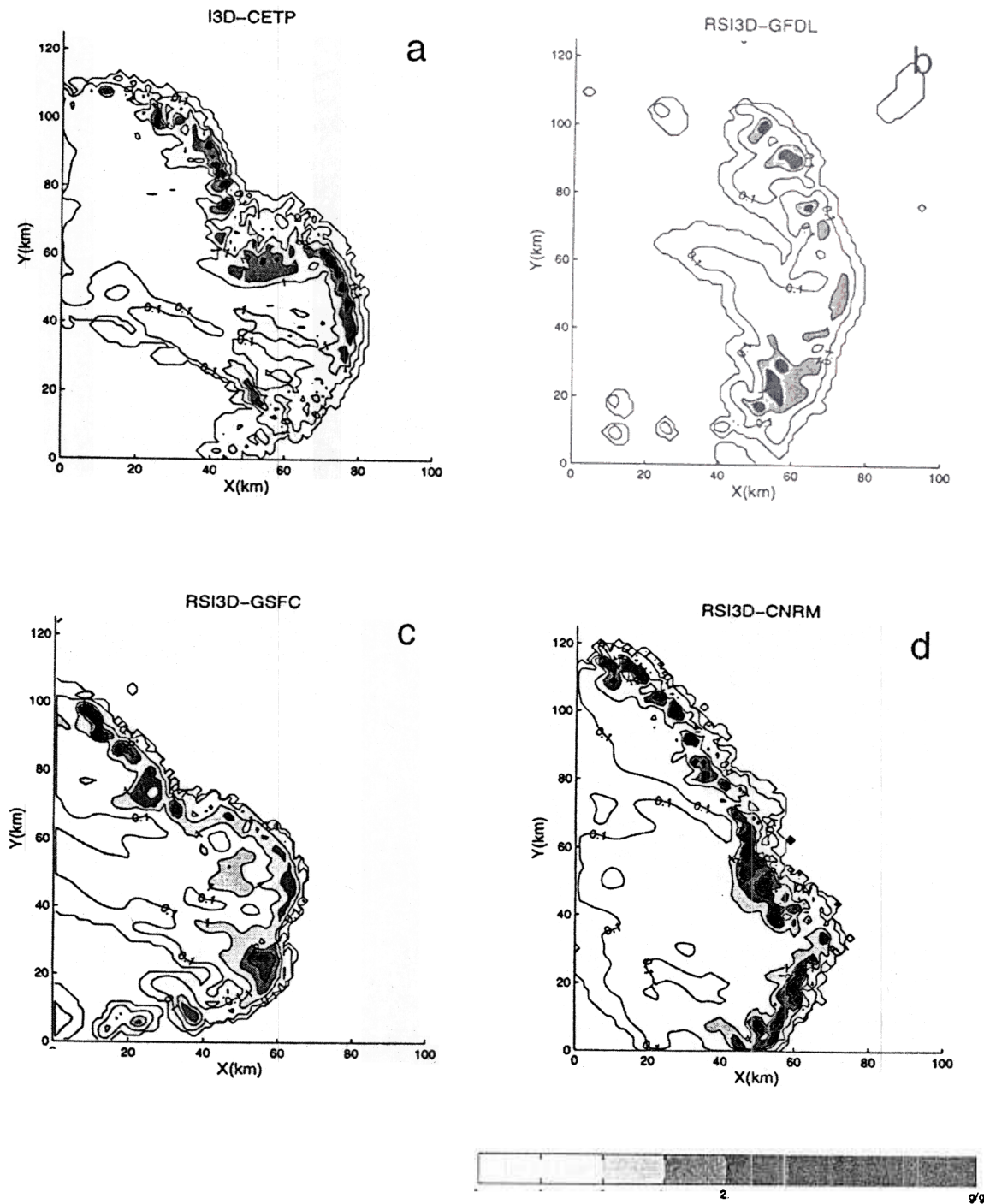


Figure 7. Horizontal cross-sections of the total hydrometeor fields (contour interval  $1.0 \text{ g kg}^{-1}$ , except that the first two isolines correspond to values of  $0.1$  and  $0.5 \text{ g kg}^{-1}$ ) after 6 hours run time and at a height of  $1.4 \text{ km}$  for runs (a) I3D (CETP), (b) RSI3D (GFDL), (c) RSI3D (GSFC), and (d) RSI3D (CNRM) (see Tables 1 and 4 for an explanation of the acronyms).

vertical velocity amplitudes in the convective cores are similar for all four 3D experiments, and their horizontal sizes are also similar. The reduction in the fractional area of the convective cells in the GFDL model, which was suggested above, is readily apparent in Fig. 8(b).

Vertical cross-sections of radar reflectivity and vertical velocity derived from two different analyses of airborne Doppler radar (Jorgensen *et al.* 1997; Montmerle and

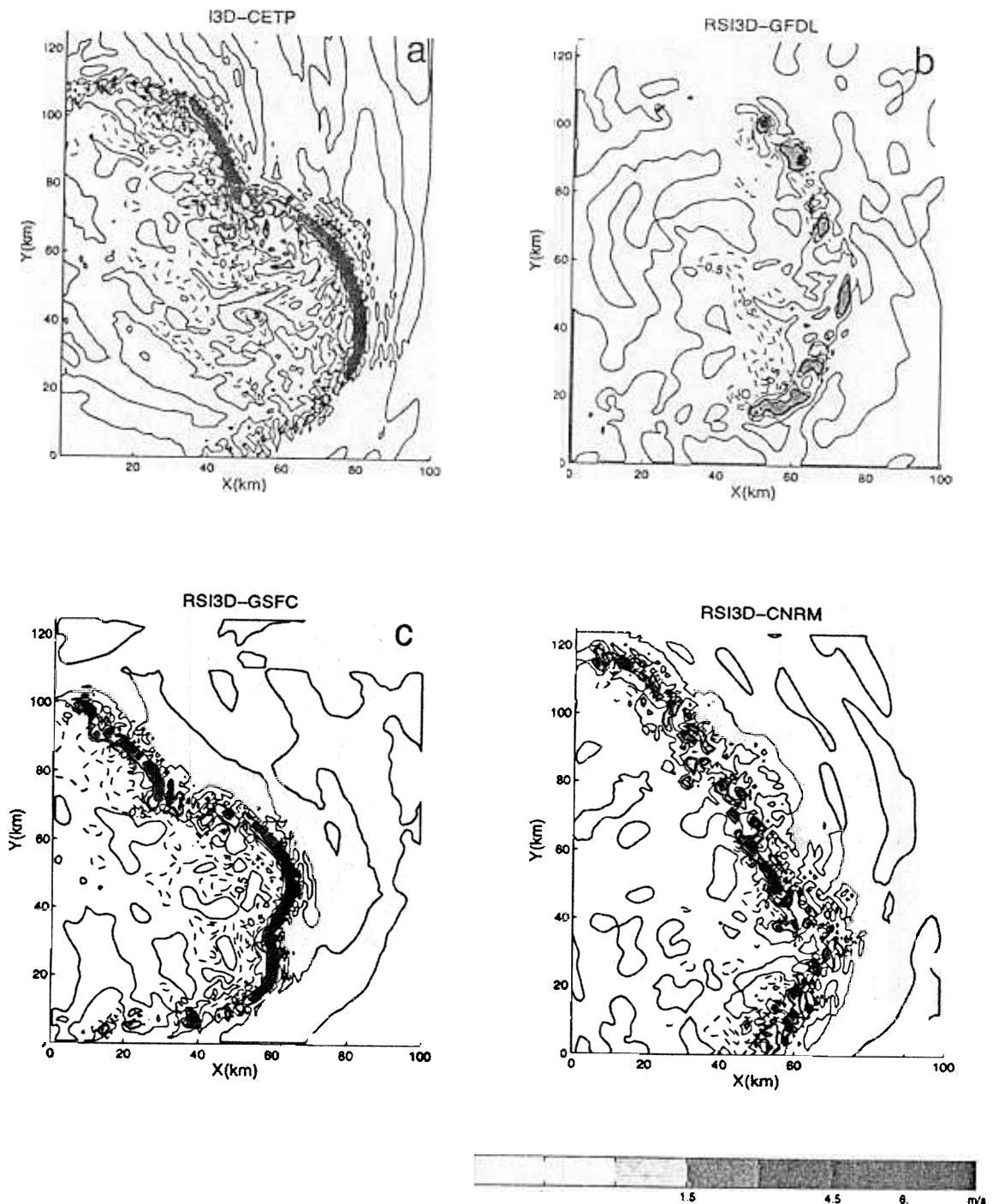


Figure 8. As Fig. 7, but for the vertical velocity (positive values (full lines) and negative values (dashed lines) with a contour interval of  $2.5 \text{ m s}^{-1}$ , except that the first continuous and dashed isolines correspond to values of  $1.0$  and  $-0.5 \text{ m s}^{-1}$ , respectively).

Lemaitre 1998) are shown in Fig. 9. The values represent averages along the central linear part of the observed squall line. In spite of the differences in analysis and averaging, these two cross-sections show very similar main features. A strong rearward and upward acceleration occurs just to the rear of the leading edge of the convection where the reflectivity is a maximum. Two distinct maxima of vertical velocity are observed: a low-level updraught up to  $z = 4 \text{ km}$  near the leading edge and an upper-level

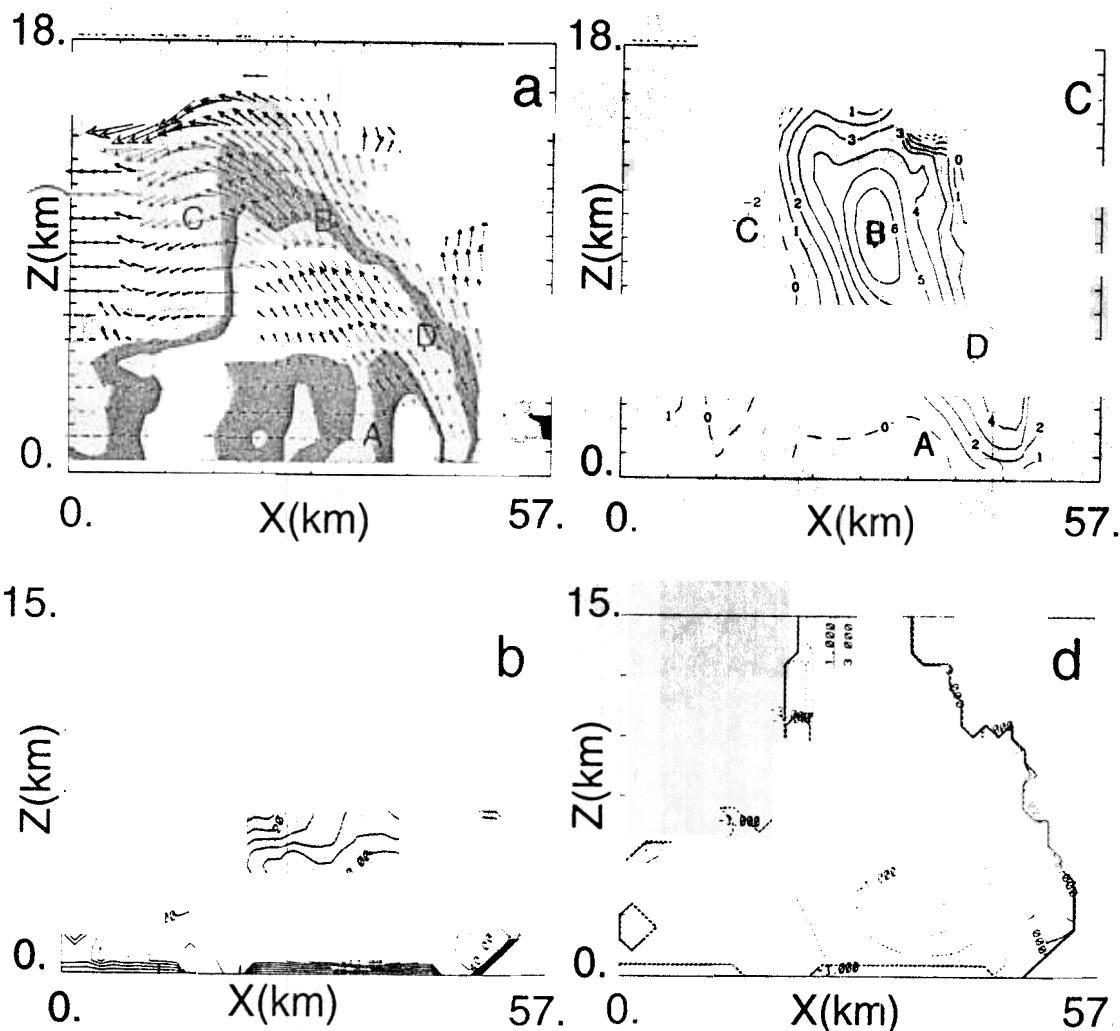


Figure 9. Vertical cross-sections (a) and (b) of radar reflectivity (dBZ, contour interval 5 dBZ), and (c) and (d) of vertical velocity ( $\text{m s}^{-1}$ , contour interval  $1 \text{ m s}^{-1}$ ) as analysed from Doppler radar observations around 2100 UTC 22 February 1993 over domains (a) and (c)  $57 \text{ km} \times 18 \text{ km}$  constructed from 40 km averages along the squall line (Jorgensen *et al.* 1997), and (b) and (d)  $57 \text{ km} \times 15 \text{ km}$  constructed from 7 km averages along the squall line (Montmerle and Lemaitre 1998). Doppler wind arrows are shown in (a).

updraught from  $z = 5$  to 15 km, 15–20 km to the rear. Another noticeable feature is the presence of weak mean downward motions at the rear of the system. The differences in the position and amplitude of the downward motions as deduced from the two methods, and the two different line-averages, can be explained to a large degree by the variability along the squall line, as illustrated by Fig. 8 and discussed by Jorgensen *et al.* (1997) and Trier *et al.* (1996). Detailed examination of the observed fields reveals that the mid-tropospheric vertical-velocity minimum is a common, but not persistent, feature of the central linear part of the squall line.

Figures 10 and 11 indicate that all the 2D and 3D simulations produce a strong maximum of total water content and vertical velocity in the convective region, as observed (Fig. 9). A rather good agreement is found between the simulated fields from the 3D models with open lateral boundary conditions in the propagation direction (CETP, CNRM and GSFC) (Figs. 10(g), (h) and (i)) and the observed fields of vertical velocity. In particular, the tilting of the updraught region, the altitudes of the low-level and upper-level maxima, and their horizontal separations closely resemble those

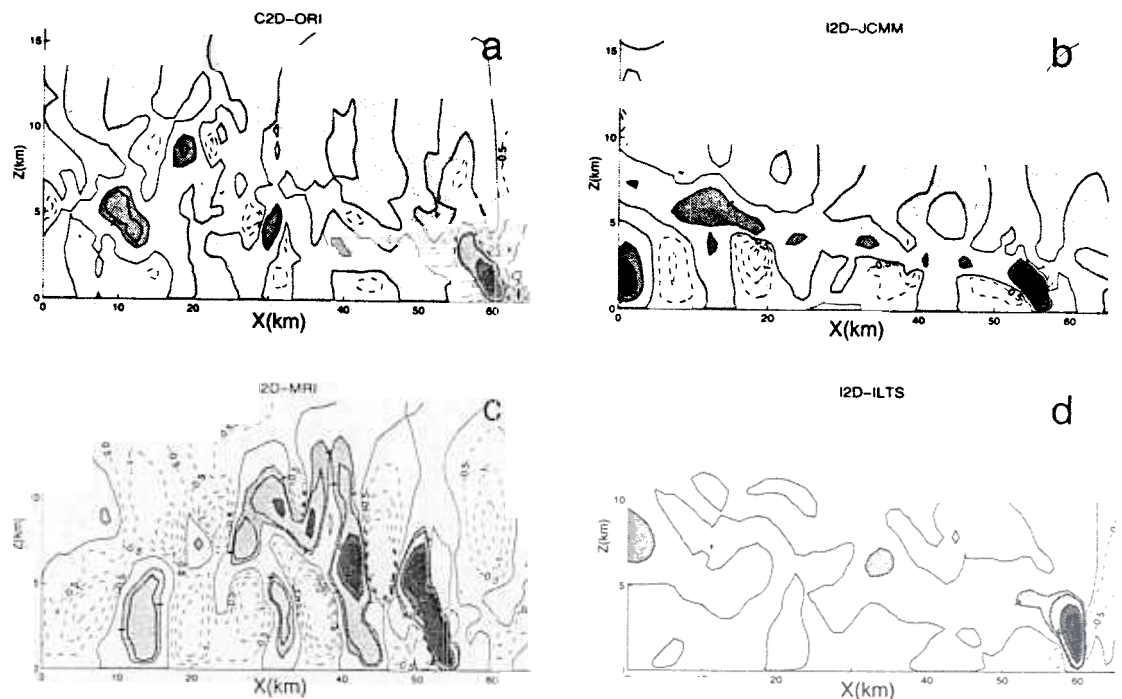


Figure 10. Vertical cross-sections of the vertical velocity ( $\text{m s}^{-1}$ , contour interval  $1 \text{ m s}^{-1}$ ) after 6 hours run time for runs (a) C2D (ORI), (b) I2D (JCMM), (c) I2D (MRI), (d) I2D (ILTS), (e) I2D (CNRM), (f) RSI3D (GFDL), (g) RSI3D (CNRM), (h) RSI3D (GSFC), and (i) I3D (CETP)—only part of the simulation domain is shown (see Tables 1 and 4 for an explanation of the acronyms).

observed. The GFDL 3D model with lateral periodic boundary conditions is able to reproduce some of these features, though with a larger tilting of the updraught region and less intense motions (Fig. 10(f)). The vertical development behind the leading convective region predicted by the 2D CRMs shows some differences from experiment to experiment. These differences occur in both the vertical velocity and the total water content fields (Figs. 10(a)–(e) and 11(a)–(e)) and seem to arise mainly from differences in the microphysical parametrizations. Nevertheless, most of the models which include an ice-phase parametrization are able to simulate the double-maxima vertical-velocity structure as observed by Doppler radar (Fig. 9) although the  $(x, z)$  locations of these maxima differ. The comparison for the 2D experiments is difficult for many reasons. For example, owing to a strong rearward flow, the JCMM and ILTS experiments produce their secondary updraught maxima in the mid-to-upper troposphere more than 50 km to the rear of the leading edge of the squall line and cannot, therefore, be seen in the figure. It is also important to stress the difficulties in the comparison of such fields owing to the large space and time variations in convective activity. The 2D simulations generally exhibit more time variability than the 3D simulations. One explanation is that the flow in the 2D models is constrained in the  $x$ – $z$  plane and lacks the observed variability along the line. Comparisons between the 2D and 3D experiments performed with the same model (CNRM) show that the spatial variability in the 3D run is replaced by time variability which is reinforced in the 2D run (not shown). This is partly illustrated by the vertical velocity field of these two experiments (Figs. 10(e) and (g)). In the 2D experiment a succession of updraughts and downdraughts is seen, contrasting with the continuous region of vertical velocity in the 3D run.

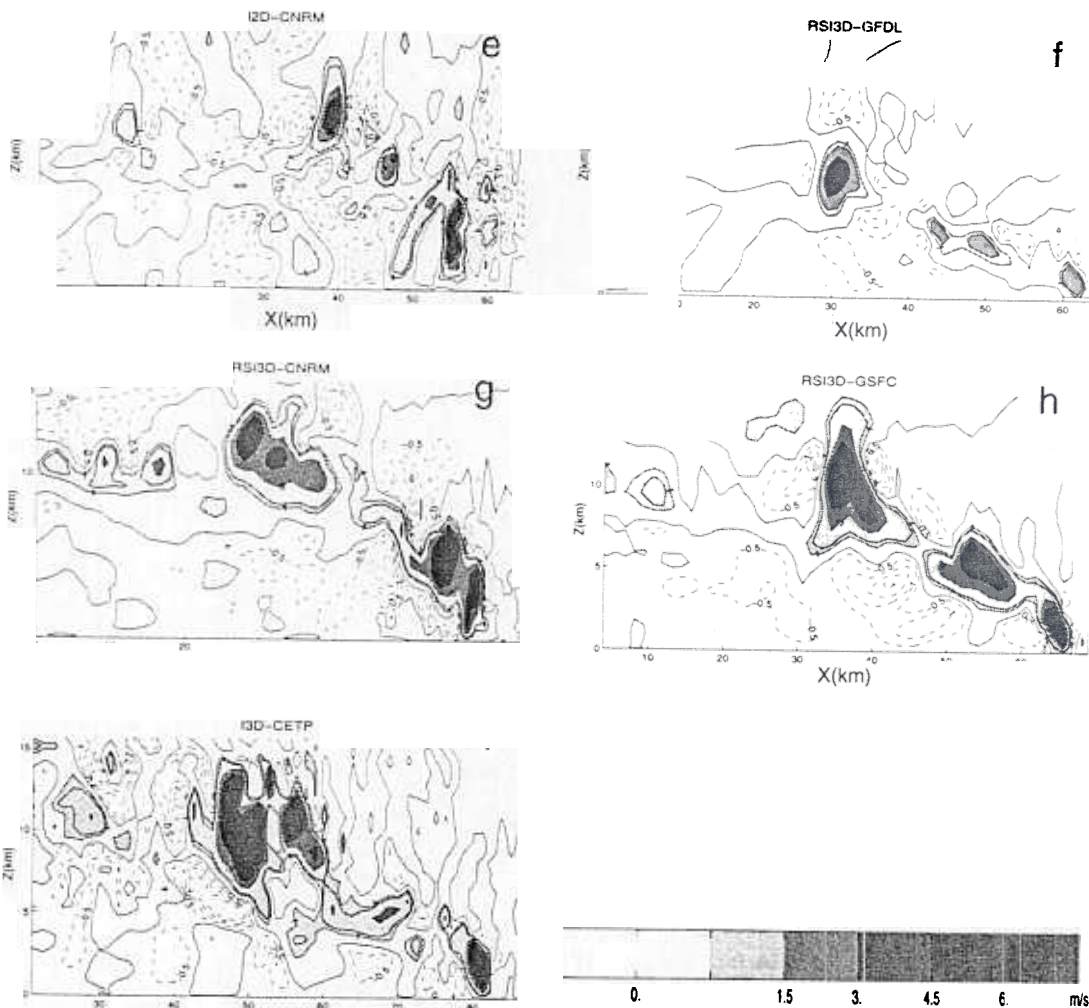


Figure 10. Continued.

Other comparisons (not shown) between the observations and the 3D simulations have been made for thermodynamic parameters. The 3D experiments are able to reproduce the amplitude and structure of the large decrease in moist static energy caused by the decrease in humidity. This feature is less well represented in the 2D experiments. One reason is that the 3D experiments have stronger updraughts and produce stronger convection-induced downdraughts causing larger drying in the cloud-free area.

### (c) Vertical profiles

Examination of the wind profiles from the 3D simulations indicates that the average effect of the convective system is to decrease the intensity of the low-level jet (Fig. 12(b)). All the 3D experiments that include the ice phase also produce an increase of the line-normal wind between 9 and 16 km related to upward motions observed in these experiments in Figs. 10(g), (h) and (i). The amplitudes of these changes in the wind are considerably less (about 5 times) than those found in previous studies of African squall lines observed during the COPT81 experiment (Caniaux *et al.* 1995). The line-parallel wind is also slightly decreased in low levels in experiments CETP and GFDL (Fig. 13). In contrast to the other 3D models, the CETP 3D experiments with and without

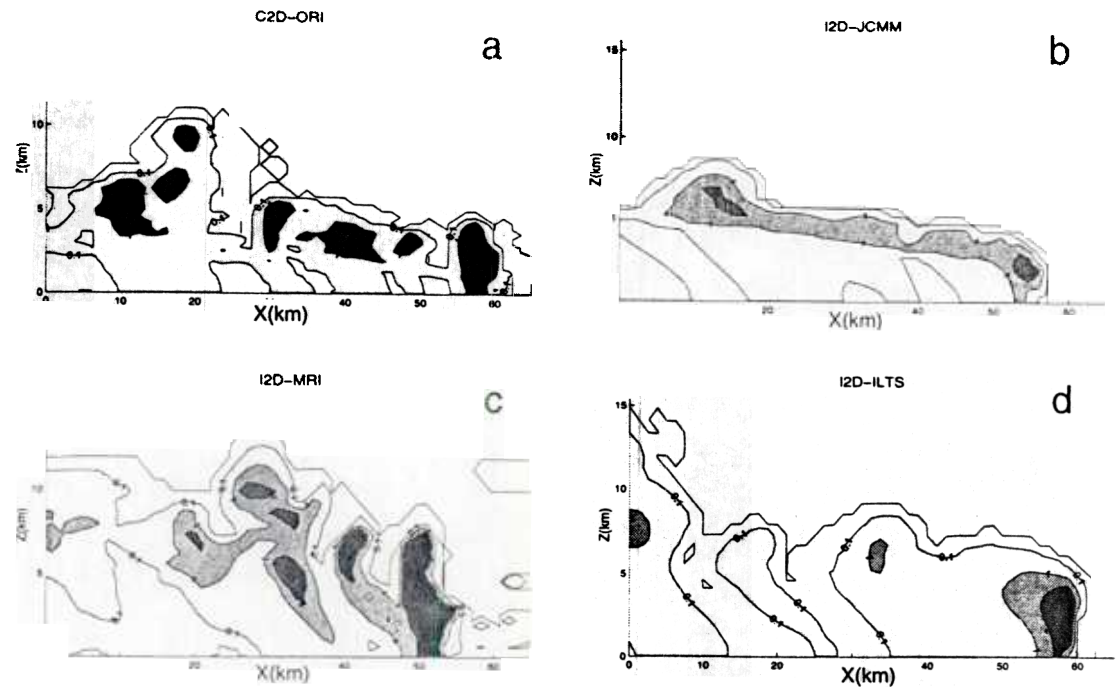


Figure 11 As Fig. 10, but for the total hydrometeor (liquid + solid) fields ( $\text{g kg}^{-1}$ , contour interval  $1.0 \text{ g kg}^{-1}$  except that the first two isolines correspond to values of  $0.1$  and  $0.5 \text{ g kg}^{-1}$ ).

an ice phase predict an increase of line-normal wind in the boundary layer. This feature is not observed and needs to be understood in the future.

All the 2D experiments exhibit an acceleration of the low-level jet which is absent in all 3D experiments (Fig. 12(a)). Above the jet, the 2D models also show vertical oscillations in the line-normal wind. The amplitude of acceleration and oscillations depends on models and convection intensity. More active convection induces larger amplitudes of acceleration and oscillations. Thus, the JCMM 2D experiments that produce more hydrometeors (Fig. 6) and rainfall (Fig. 4) than other 2D models have the largest oscillations. The 2D experiments with no ice phase (less active) have the smallest oscillations. The different behaviour of line-normal wind, as predicted by the 2D and 3D models, can be analysed as follow. Horizontal cross-sections of the simulated squall lines (Figs. 7 and 8) clearly display the three-dimensional character of the flow, both at the convective-cell scale and the system scale. In particular, the structure of the horizontal flow (not shown) shows an asymmetric structure over a significant part of the system, with a tendency to form vortices at the northern and southern parts of the squall line. These features were clearly observed in the northern part by Doppler radars (Jorgensen *et al.* 1997). The central part exhibits flow acceleration relative to the other parts. The northern and southern parts of the system have an orientation which differs from the low-level environmental shear, and the momentum transports consequently differ. To a first approximation, the flow structure in the central part of the squall line is quasi-2D and, in this limited part of the system, the 3D simulations produce an increase in the line-normal shear which is well reproduced by the 2D simulations. The origin of vertical oscillations in the 2D simulations can then be explained by considering the anelastic continuity equation in a 2D framework:

$$\frac{\partial \rho u(x, z, t)}{\partial x} + \frac{\partial \rho w(x, z, t)}{\partial z} = 0. \quad 1$$

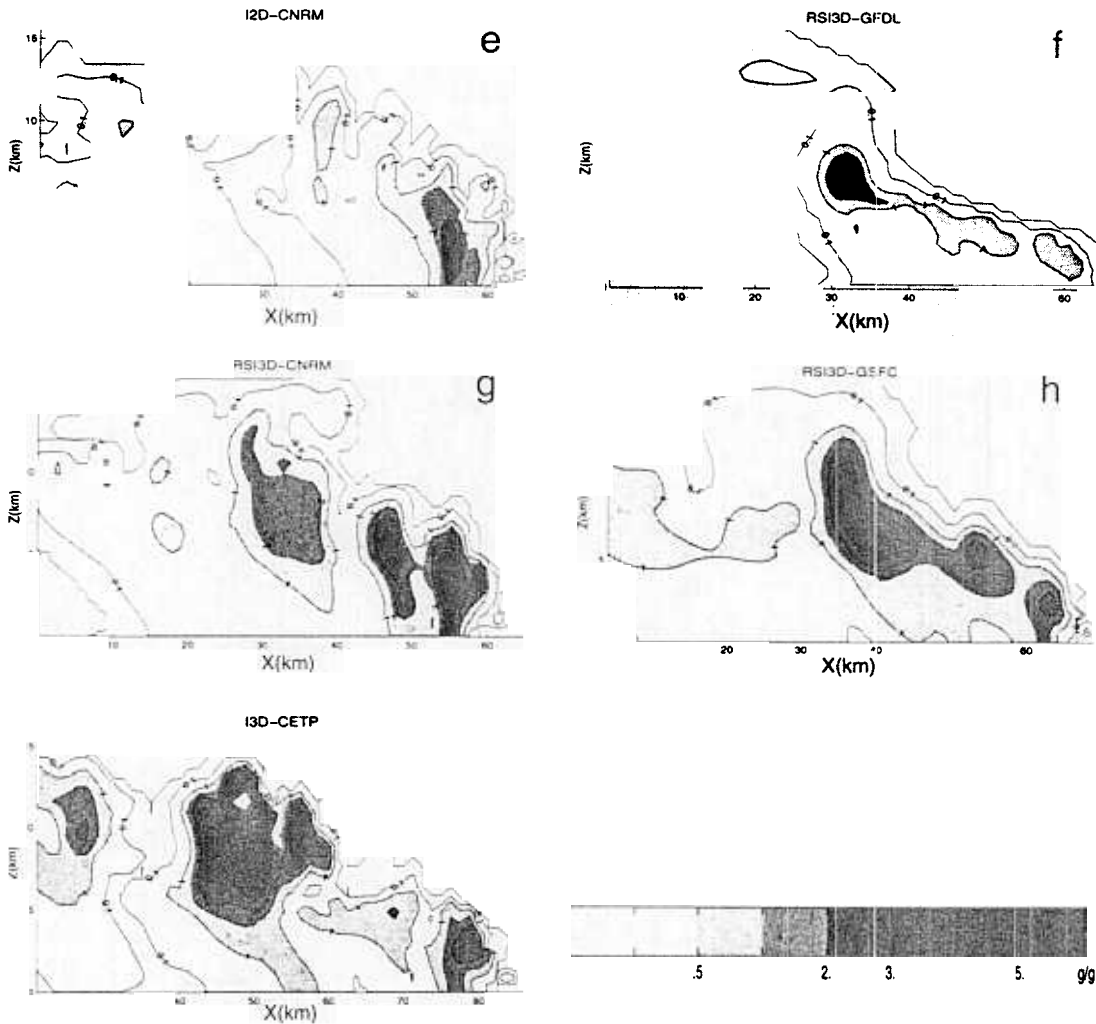


Figure Continued.

Integrating this equation from the bottom to the top of the model domain, where the vertical velocities are specified to vanish, the following integral constraint is obtained:

$$\frac{\overline{\partial \rho u(x, t)^H}}{\partial x} = \frac{1}{H} \int_0^H \frac{\partial \rho u(x, z, t)}{\partial x} dz = 0. \quad (12)$$

Thus, the vertical average of  $u$ -momentum is independent of  $x$  and can only change with time. As quoted by Fovell and Ogura (1988), at each time step each elementary column of the 2D model contains the same amount of  $u$ -momentum. Moreover, with periodic lateral boundary conditions (JCMM), this column-integrated  $u$ -momentum cannot change in time if no friction is allowed at the surface (as specified in this intercomparison). With open lateral boundary conditions, it can evolve depending on the exact treatment of these boundary conditions. Assuming that outside the cloud system the  $u$ -momentum is unchanged (or only weakly modified), the above equation means that, owing to the acceleration of the low-level jet in the convective columns, a compensating deceleration has to be produced. The amplitude of the resulting vertical oscillations will thus depend on the intensity of the convection at the origin of the low-level acceleration. In the 3D numerical framework, as in nature, the integral constraint

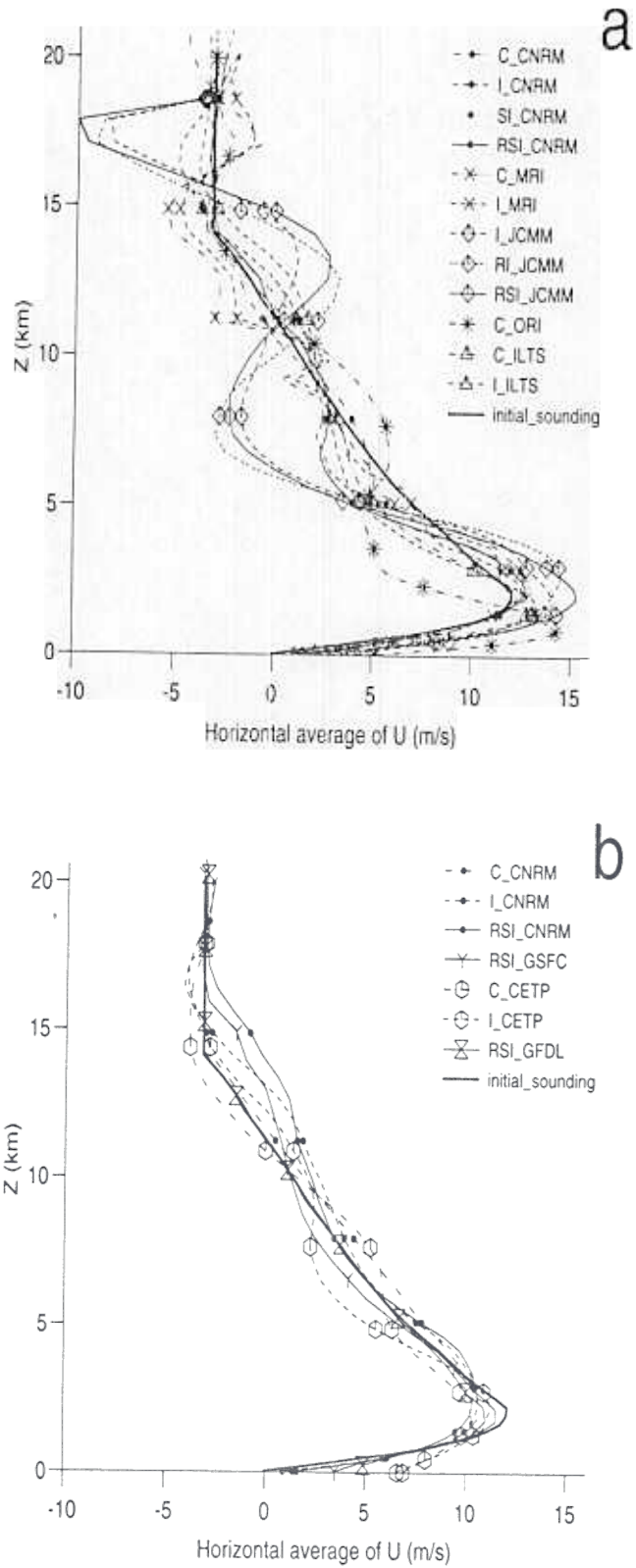


Figure 12. Vertical profiles of the  $u$  (squall-line normal) component of the wind (m s<sup>-1</sup>) averaged from 5 to 6 h of (a) the 2D cloud-resolving model (CRM) simulations, and (b) the 3D CRM simulations (see Tables 1 and 4 for an explanation of the acronyms).

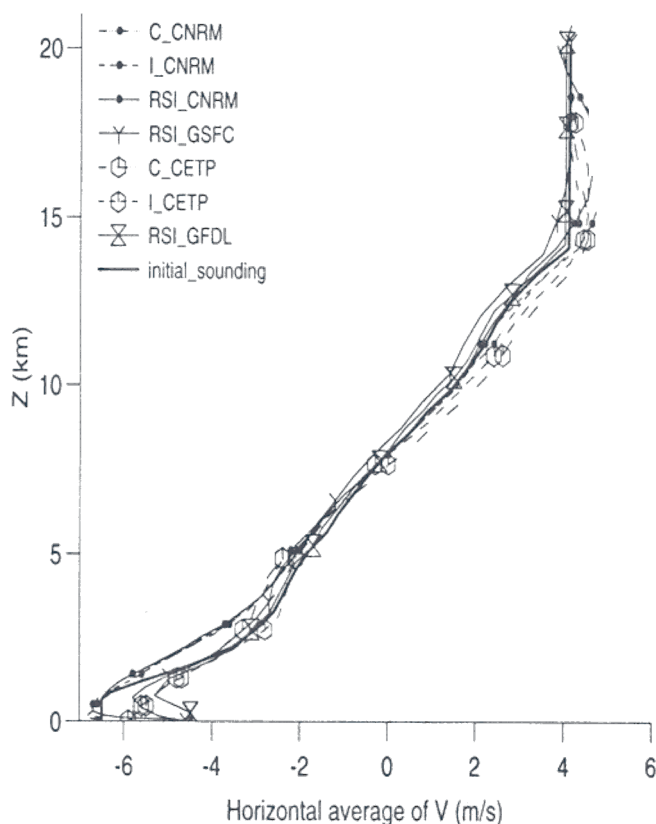
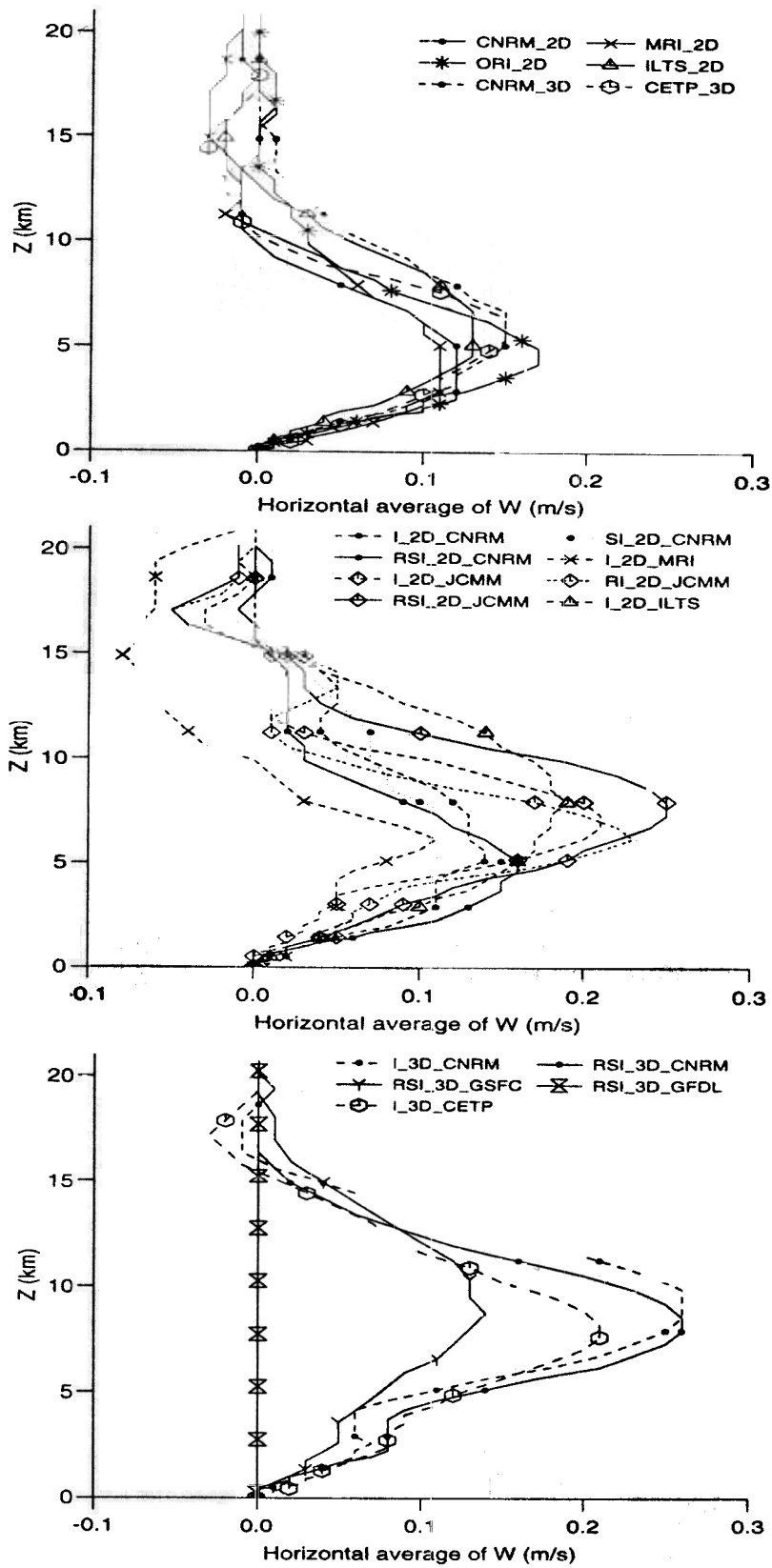


Figure 13. Vertical profiles of the  $v$  (squall-line parallel) component of the wind ( $\text{m s}^{-1}$ ) averaged from 5 to 6 h of the 3D cloud-resolving simulations (see Tables 1 and 4 for an explanation of the acronyms).

also involves the  $v$ -momentum; so with more degrees of freedom the 3D models do not exhibit these large vertical oscillations.

Vertical profiles of mean vertical velocity simulated by models without an ice phase (Fig. 14(a)) show very similar qualitative and quantitative values, with a well defined maximum of  $0.15 \text{ m s}^{-1}$  around  $z = 4 \text{ km}$ . In contrast, 2D experiments with an ice phase (Fig. 14(b)) exhibit more variation from model to model. It is likely that these variations are due to differences in the ice-phase parametrizations. Both the ILTS and the JCOMM 2D experiments that include an ice phase show a maximum at a higher level (between 6 and 8 km) than other 2D experiments with ice-phase parametrizations, a feature which corresponds more closely to observations (Fig. 9). The effects of the ice phase are better viewed in Fig. 15(a) which shows the differences between experiments with and without an ice phase for the same models (CNRM and ILTS). The main effect is clearly to increase the vertical motion between 5 and 16 km. This effect is about twice as large in the 3D than in the 2D experiments. Vertical profiles of the mean vertical velocities from the 3D experiments (Fig. 14(c)) show a maximum at around 8 km with a value of  $0.27 \text{ m s}^{-1}$  for CNRM and CETP 3D models running with open lateral boundary conditions. Note that periodic lateral boundary conditions require the domain-average vertical velocity to be zero for the GFDL model. The GSFC model produces smaller vertical velocities than the CNRM and CETP models, probably due to the use of periodic lateral boundary conditions along the  $y$ -direction. The shape, nevertheless, exhibits similar features, such as the characteristic double-peak structure seen in the vertical-velocity cross-sections (Fig. 10(g), (h) and (i)). Comparisons between the 2D and 3D experiments (dashed lines in Fig. 15(a)) for the CNRM model clearly show



C

Figure 14. Vertical profiles of vertical velocity ( $\text{m s}^{-1}$ ) averaged from 5 to 6 hours of (a) the 2D and 3D cloud-resolving model (CRM) simulations with no ice-phase parametrization, (b) the 2D CRM simulations with an ice-phase parametrization, and (c) the 3D CRM simulations with an ice-phase parametrization (see Tables 1 and 4 for an explanation of the acronyms).

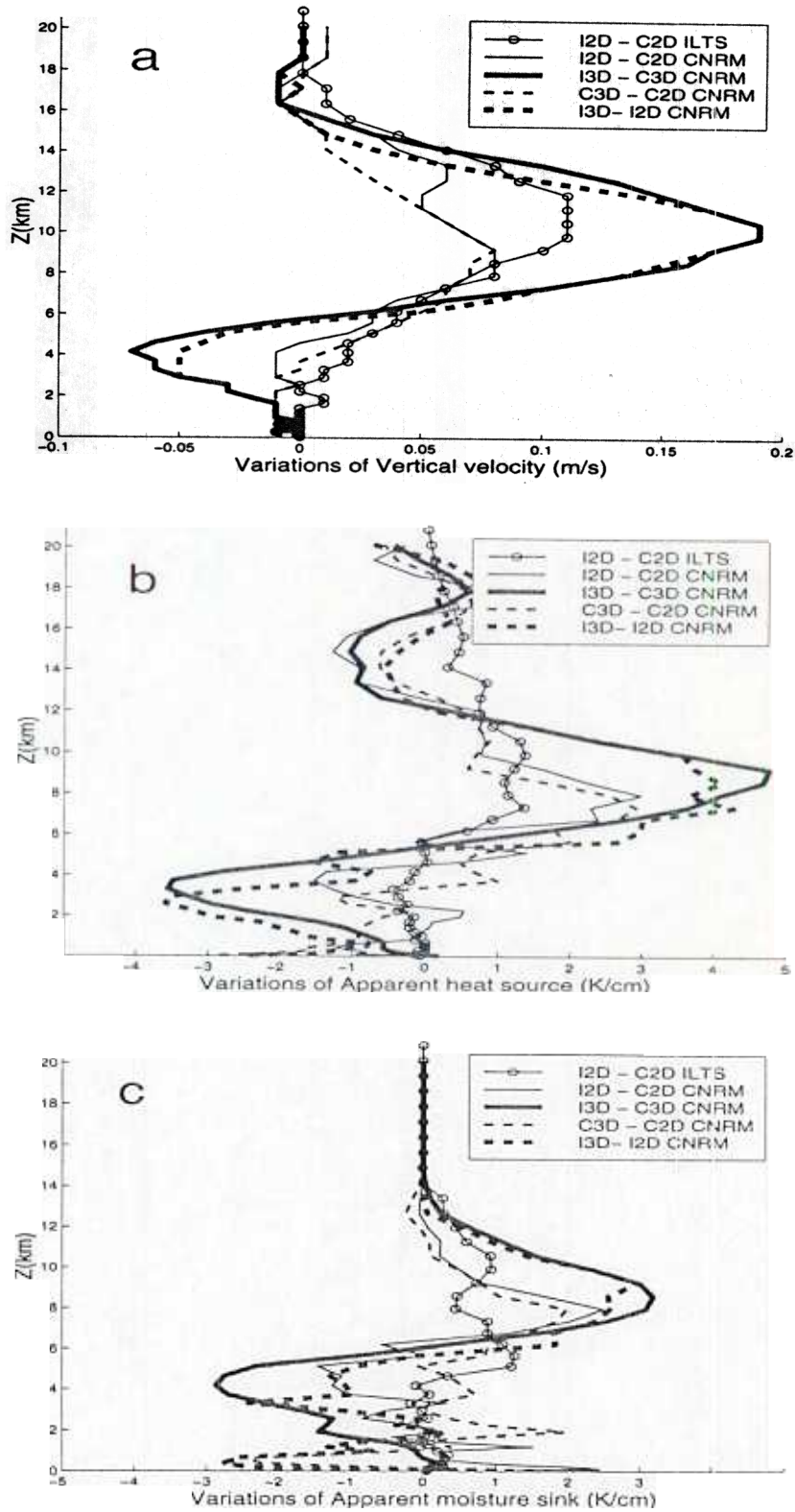


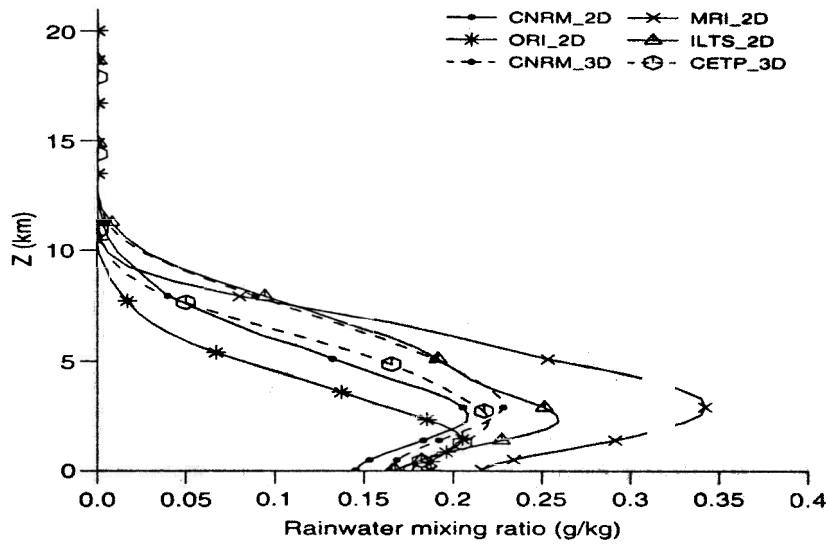
Figure 15. Differences between experiments illustrating the effects of ice-phase parametrizations and dimensionality. (a) The vertical velocity ( $m s^{-1}$ ), (b) the apparent heat source normalized by the total surface rainfall ( $K cm^{-1}$ ), and (c) the apparent moisture sink normalized by the total surface rainfall ( $K cm^{-1}$ ). The solid lines show the differences between experiments with and without an ice-phase parametrization, and the dashed lines show the differences between the 3D and 2D experiments (see Tables 1 and 4 for an explanation of the acronyms).

that the inclusion of the third dimension has an effect similar in shape and amplitude to that of including the ice phase (solid lines in Fig. 15(a)). The main effect is clearly to increase the vertical motion (up to 0.08 and 0.2  $\text{m s}^{-1}$  for no-ice and ice experiments, respectively) between the heights of 5 and 16 km. A more surprising result is the decrease observed below 5 km in the 3D run that includes an ice phase compared with the results from the 2D run with ice and the 3D run without ice. This shows that both the ice-phase parametrization and three-dimensionality are important. Also, the effects are not simply additive as no such effect is observed when the ice phase is added in the 2D runs for both the ILTS and the CNRM models, and when the third dimension is added for the CNRM model without an ice phase. Looking at the same profiles, but in the convective and stratiform regions (not shown), reveals that the differences come mainly from the stratiform region where the motions are more intense in the 3D models than in the 2D models. The larger development of the stratiform region in experiments including the ice phase explain the increase of both upward and downward motions present in the stratiform region.

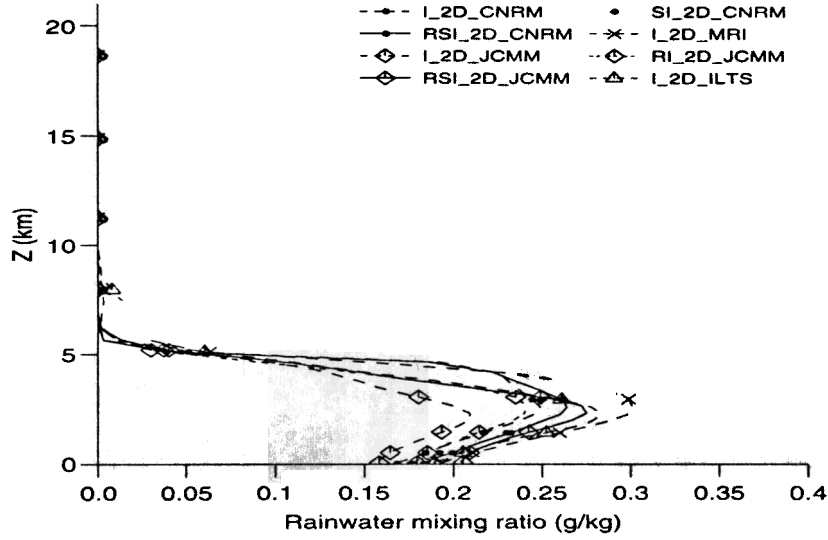
Typical vertical profiles of the rain water content are shown in Fig. 16. The maxima are found at altitudes between about 3 and 4 km in models both with and without an ice phase, and have similar values in each case. This suggests that much of the precipitation is generated by 'warm-rain' processes between the cloud base and the melting level, which is at around 5 km. The 3D experiments with an ice phase tend to show the rain maximum at a higher altitudes than comparable 2D experiments. This suggests the organization of precipitation differs in the 3D models. The vertical velocity fields (Fig. 10) show indeed that the second core of the updraught is generally more delayed in the 2D than in the 3D runs. In addition, the updraughts are more intense in the 3D runs than in the 2D runs (Fig. 3), resulting in a larger production of ice particles in the 3D runs. Rain produced from iced hydrometeor melting is then larger in the 3D than in the 2D models. This also contributes towards producing the rain maximum at a higher altitude. In all experiments, below the level of maximum rain the vertical transport and evaporation contribute to give a negative gradient approximately equal to  $0.02 \text{ kg kg}^{-1} \text{ m}^{-1}$ .

The cloud vertical structure and cloud-top altitude for ice and no-ice experiments are contrasted by comparing the profiles of total water content (liquid + solid). As shown in Fig. 17, all the no-ice simulations have their maximum total hydrometeor content well below the melting level, whereas the ice-phase models have the maximum at or above the melting level. Cloud tops are lower in the experiments without an ice phase (around 12 km) than in experiments with an ice phase (around 16 km). Most of the profiles of total water content from experiments with ice (Figs. 17(b) and (c)) give qualitatively similar profiles, with an increase from 0 at  $z = 5 \text{ km}$  up to a mean value of  $0.4 \text{ g kg}^{-1}$  and then a decrease above, as with the profile of rain water content (Figs. 16(b) and (c)). There are, however, larger variations in the maximum values of total water content than in the rain water content. In particular, the MRI and JCMM 2D models predict maximum values between  $0.55$  and  $0.7 \text{ g kg}^{-1}$  although, as noted above, the JCMM model is strongly sensitive in this aspect to the ice-particle mean fall-speed.

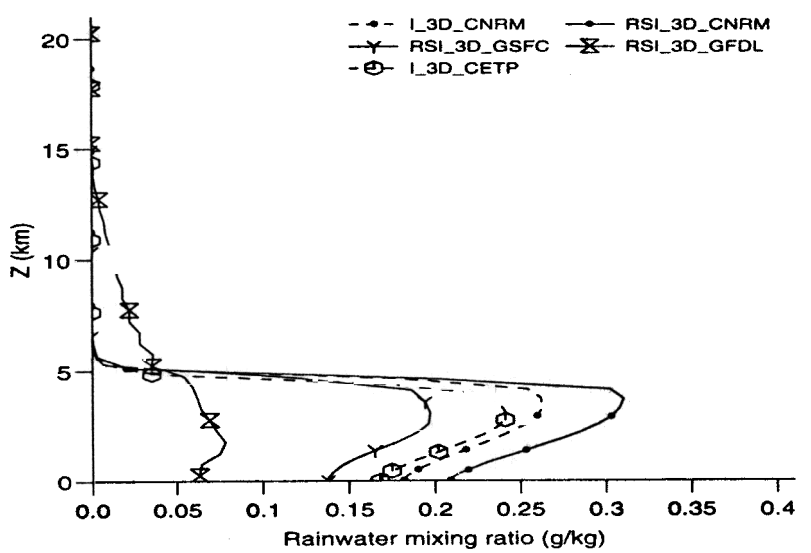
Looking only at the ice experiments, large differences in ice contents aloft (above the melting level) are likely to have a significant impact in long-duration simulations in which radiative feedbacks play a major role in the evolution of the cloud system (e.g. Krueger 1998). These differences need to be investigated further. Comparison of total water contents for the 2D CNRM and ILTS experiments with and without an ice-phase parametrization indicates slight changes in the first 5 km, and much greater values for



a

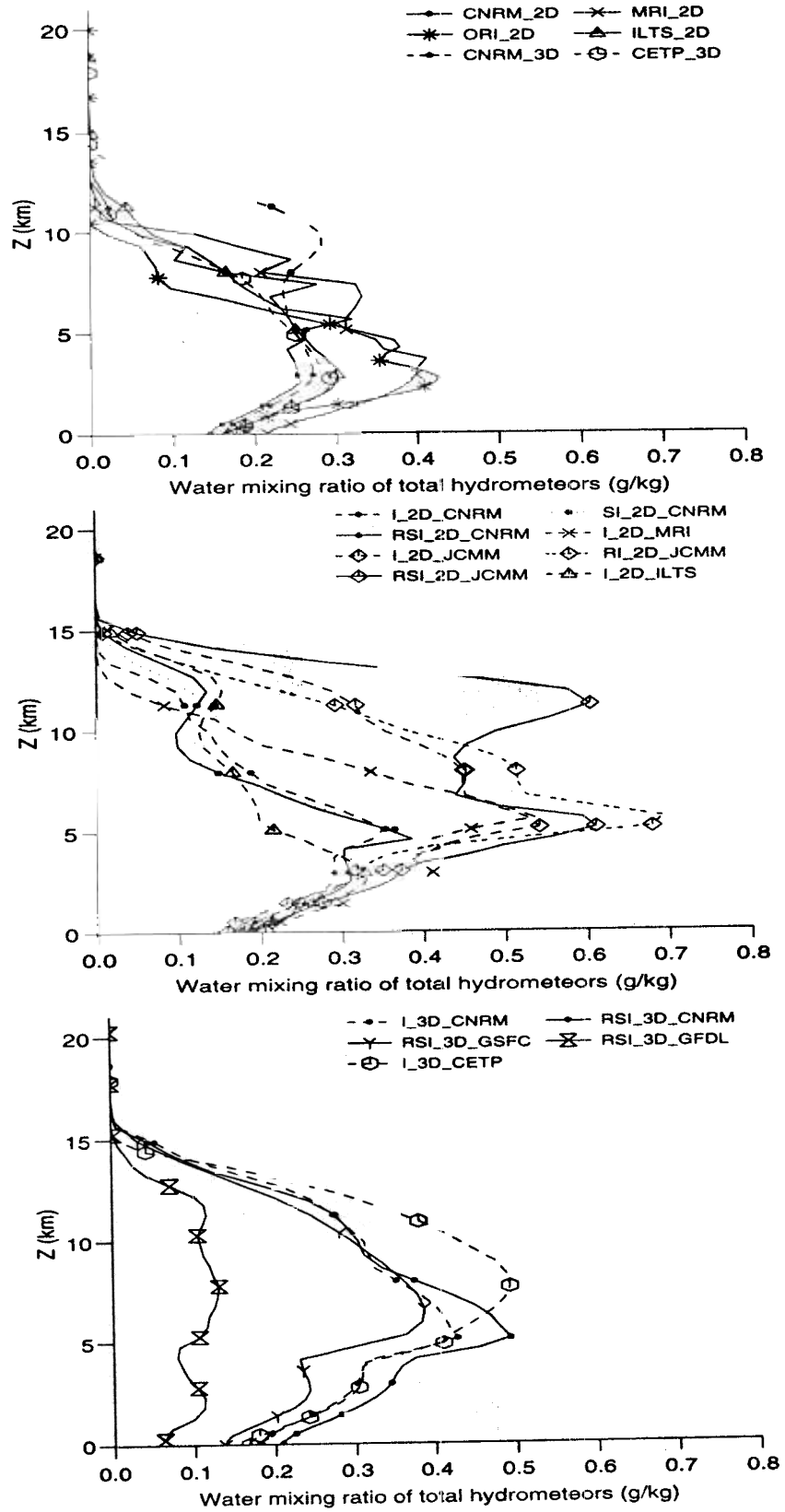


b



c

Figure 16. As in Fig. 14, but for the rain water content ( $\text{g kg}^{-1}$ ).



C

Figure 17. As in Fig. 14, but for the total water content (liquid + solid) ( $\text{g kg}^{-1}$ ).

the ice runs aloft. The latter effect can be related to the increase of vertical velocity as shown above.

Figures 16(c) and 17(c) both show that the 3D GFDL simulation with periodic lateral boundary conditions along both horizontal directions produces lower mixing ratios for rain and total hydrometeors than the 3D simulations with open boundary conditions. As discussed previously, this behavior is consistent with the absence of a feedback between the scale of the convective system and larger scales. This absence results from the periodic lateral boundary conditions, which preclude the development of destabilizing domain-averaged vertical motions (Fig. 14). Differences in model microphysical formulations could also explain some of the differences. However, the model with periodic lateral boundary conditions has also been used to simulate a composite easterly wave in the tropical east Atlantic (Donner *et al.* 1999). In this latter simulation, the effects of vertical motions at scales larger than the convective system were imposed through tendencies in the domain-averaged temperature and humidity fields. Precipitation was within 30% of observed values. Therefore, it is very likely that most of the differences in the precipitation and hydrometeors in Figs. 4(c), 5(c), 6(c), 16(c), and 17(c) arise from the imposition of periodic lateral boundary conditions along both horizontal directions on a relatively small domain.

#### (d) *Impacts on the large scale*

One of the main underlying uses of sophisticated CRMs is to be able to diagnose the effects of mesoscale convective systems on the atmosphere. Furthermore, the datasets generated by CRMs can be used to evaluate in detail the different aspects of cloud parametrizations used in GCMs (see Bechtold *et al.* 1999). Using Eqs. (5) and (6), the apparent heat and moisture sources ( $Q_{1C}$  and  $Q_2$  respectively) due to convection have been computed from the CRM output for different parts of the system. In the present paper, only the total sources normalized by the total surface rainfall are presented. The units are expressed in  $(\text{K day}^{-1})(\text{cm day}^{-1})^{-1}$  (or, equivalently, in  $\text{K cm}^{-1}$ ).

Previous studies (e.g. Lafore *et al.* 1988; Tao *et al.* 1993) have shown that squall lines produce two main effects, namely a strong heating in the free troposphere plus a cooling in the boundary layer. As shown in Fig. 18, all experiments exhibit this overall behaviour of the apparent heat source. All models predict a cooling at low levels which is of order  $1\text{--}2 \text{ K cm}^{-1}$  (normalized by the rainfall) caused by rain evaporation, as previously discussed. However, the vertical profile of heating shows variations from experiment to experiment and from model to model. The inclusion of an ice parametrization is important in determining the profiles of  $Q_{1C}$ . By releasing additional latent heat of fusion and generating stronger updraughts, the main effect is to create a second maximum of  $Q_{1C}$  at a higher altitude. As with previous profiles, differences in the profile of  $Q_{1C}$  for similar experiments can be related to differences in ice-phase parametrization used in each model.

More insight into the effect of ice schemes can be obtained by looking at the differences for the same model (ILTS and CNRM) with and without an ice-phase scheme (Fig. 15(b)). The ice phase decreases  $Q_{1C}$  below 5 km and increases it between 5 and 12 km. The amplitude of the variations is different between models, and larger in 3D than in 2D. Comparisons between the 2D and 3D experiments (Fig. 15(b)) for the CNRM model show that taking into account the third dimension has an effect similar in shape and amplitude to that of including an ice-phase parametrization, at least between 5 and 12 km. The main effect is to increase the apparent heat source (up to 3 and  $4.5 \text{ K cm}^{-1}$  for the no-ice and ice experiments) between 5 and 12 km.

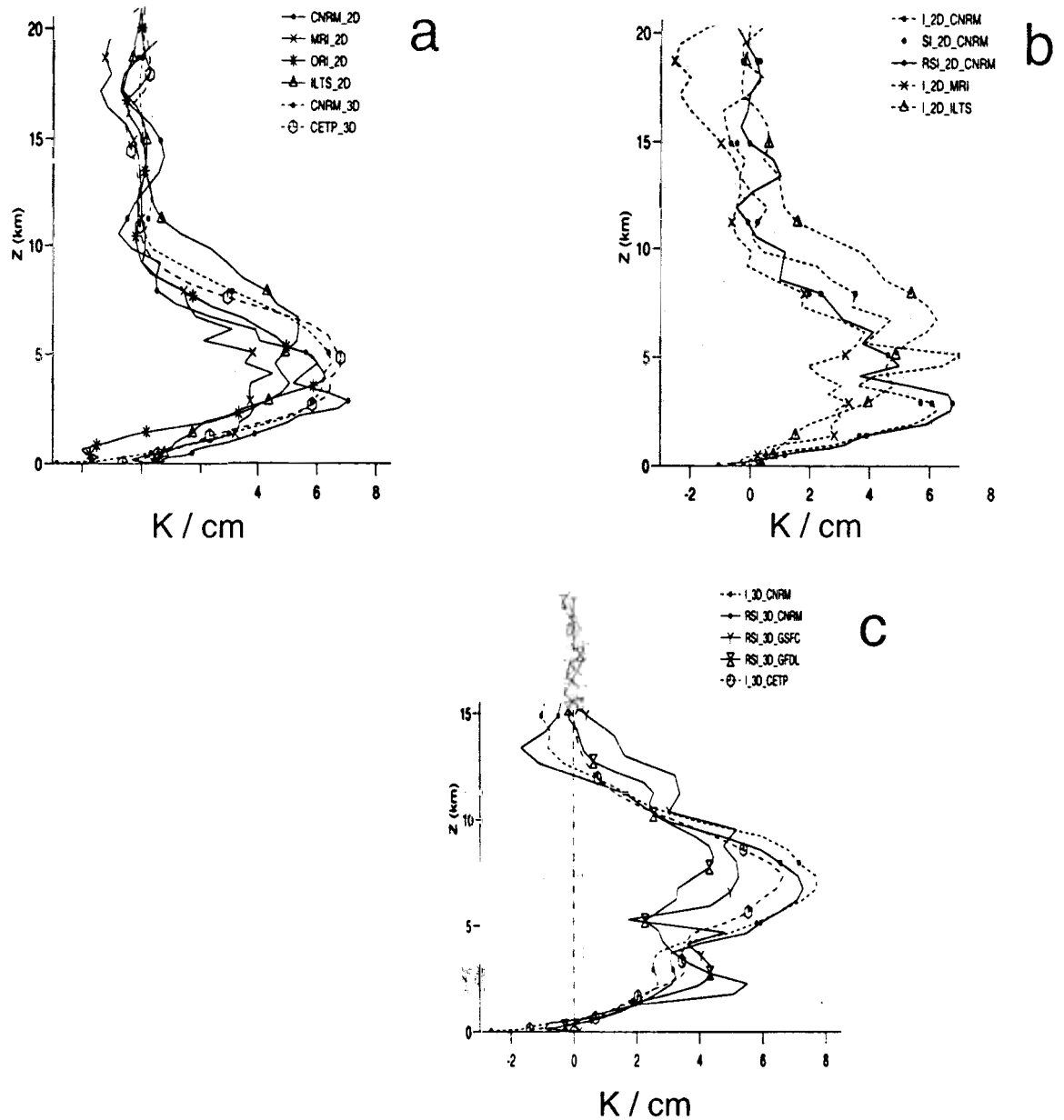


Figure 18. As Fig. 14, but for the apparent heat source normalized by the total surface rainfall ( $K \text{ cm}$ )

As with the vertical velocity profile, a decrease is observed below 5 km in the 3D run with an ice phase in comparison with both the 2D run with ice and the 3D run with no ice. The inclusion of both the ice-phase parametrization and three-dimensionality is important for determining the profile of  $Q_{1C}$ . These differences originate mainly from changes in the stratiform region since the convective region is dominated by liquid-phase precipitation production below the freezing level. These features can be directly related to the differences in the profiles of vertical velocity as discussed above (Fig. 15(a)).

Similar results to  $Q_{1C}$  are obtained when comparing the vertical profiles of apparent moisture sinks,  $Q_2$ , normalized by the total surface rainfall (Fig. 19). All models predict a drying of the atmosphere. One difference is at near-surface levels where some models predict no moistening whereas some 2D models predict moistening in the boundary layer. Overall, the differences are larger for  $Q_2$  than for  $Q_{1C}$ . A rather good agreement

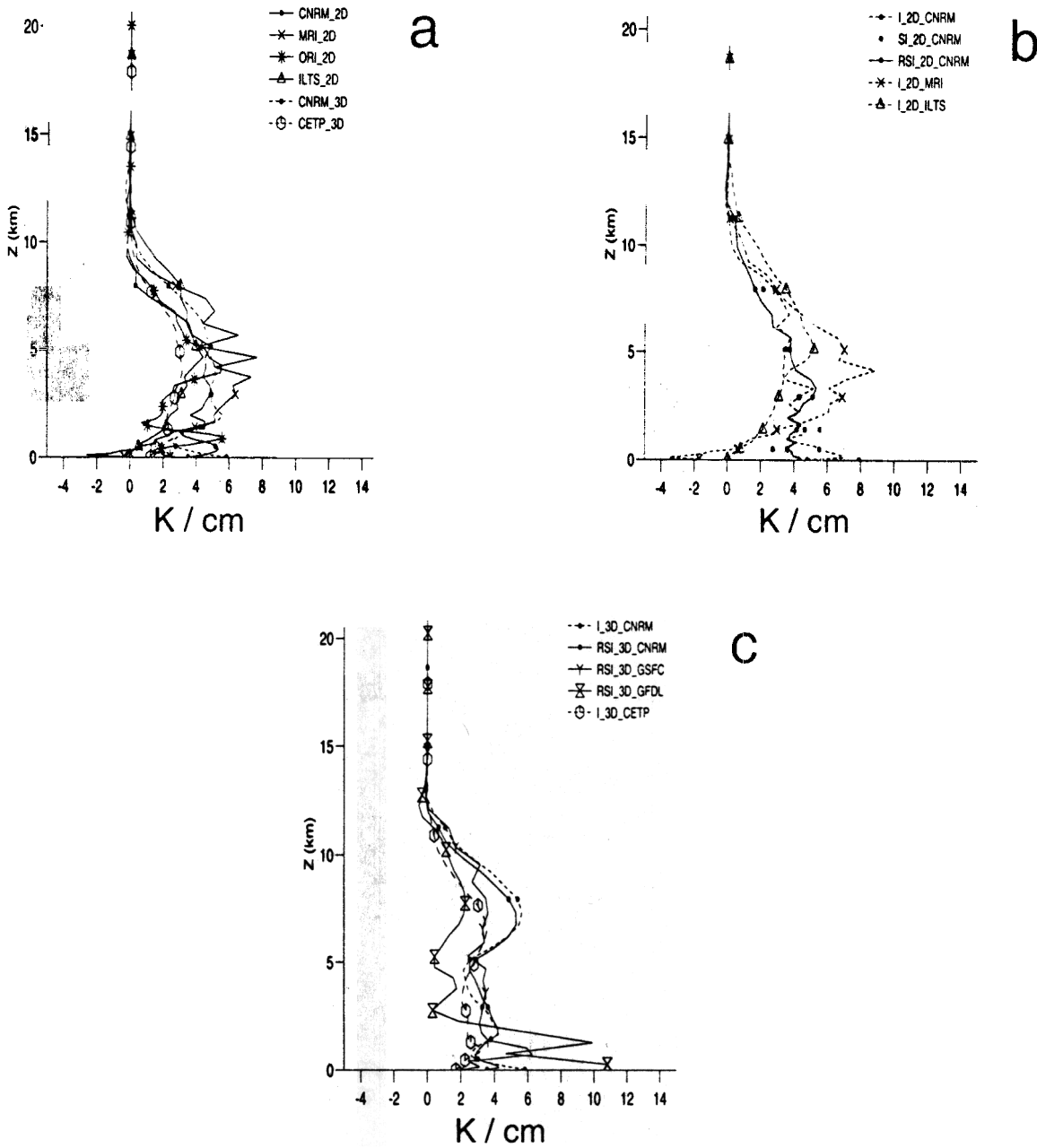


Figure 19. As Fig. 14, but for the apparent moisture sink normalized by the total surface rainfall ( $K \text{ cm}^{-1}$ ).

is, however, obtained for the 3D experiments using open lateral boundary conditions in both horizontal directions (CETP and CNRM), and less quantitative agreement with the experiment with open lateral boundary conditions in the propagation direction only (GSFC). For the reasons detailed above, the 3D experiment with periodic boundary conditions in both horizontal directions (GFDL) produced a lower amplitude of  $Q_2$ . The same remarks on the effects of ice phase and dimensionality on  $Q_{1C}$  can be made for  $Q_2$  in looking at differences between specific experiments (Fig. 15(c)). The differences occur below 3 km where the effects are quantitatively different.

In contrast to the general agreement of  $Q_{1C}$  and  $Q_2$  profiles, there are significantly different results for the net momentum transport produced by the squall line (Figs. 20 and 21). Whilst all 3D simulations give similar results, the 2D simulations produce more

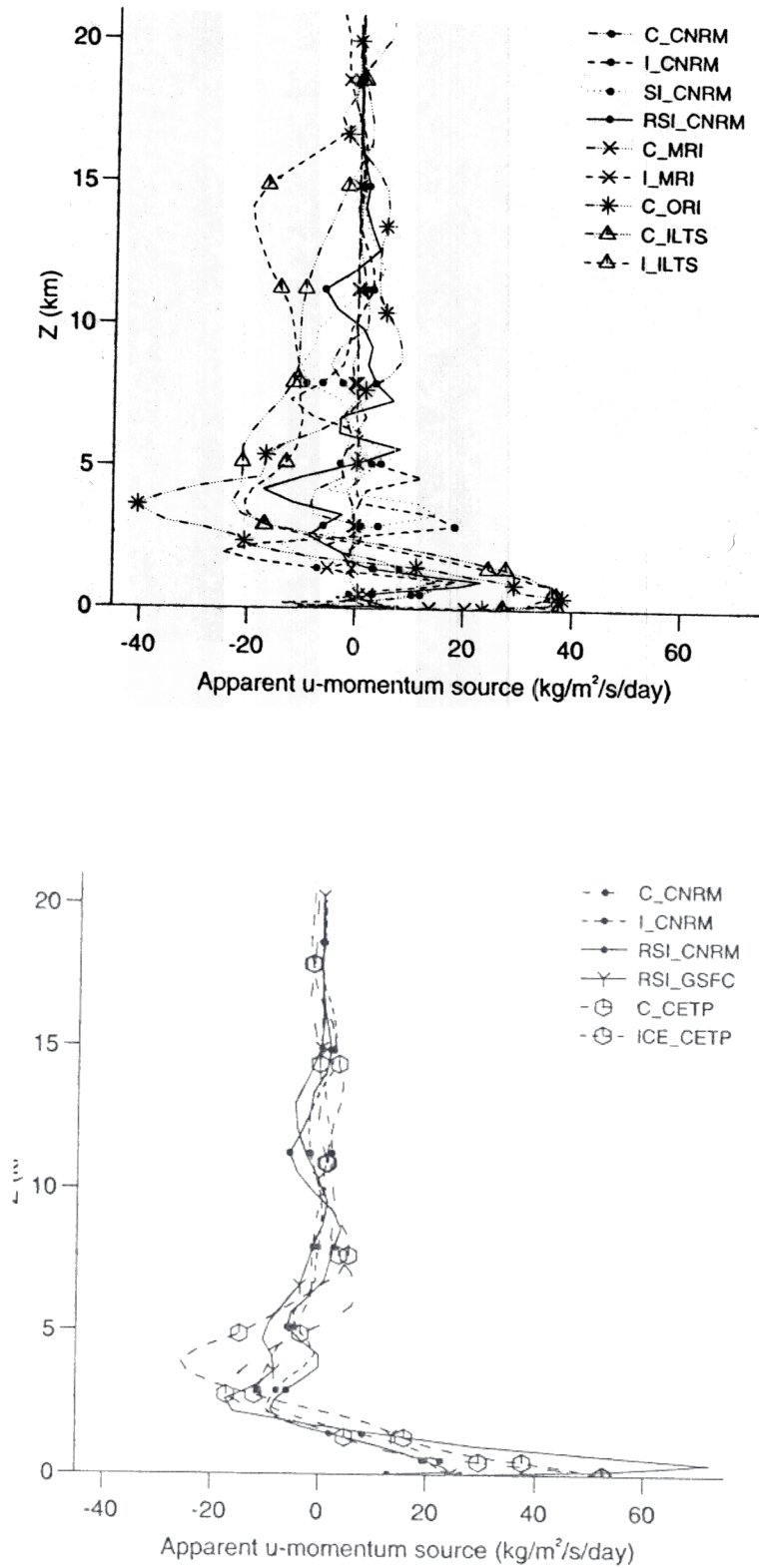


Figure 20. The vertical profiles of the  $u$  (squall-line normal) momentum source ( $\text{kg m}^{-2}\text{s}^{-1}\text{day}^{-1}$ ) averaged from 5 to 6 hours of (a) the 2D cloud-resolving model (CRM) simulations, and (b) 3D CRM simulations (see Tables 1 and 4 for an explanation of the acronyms).

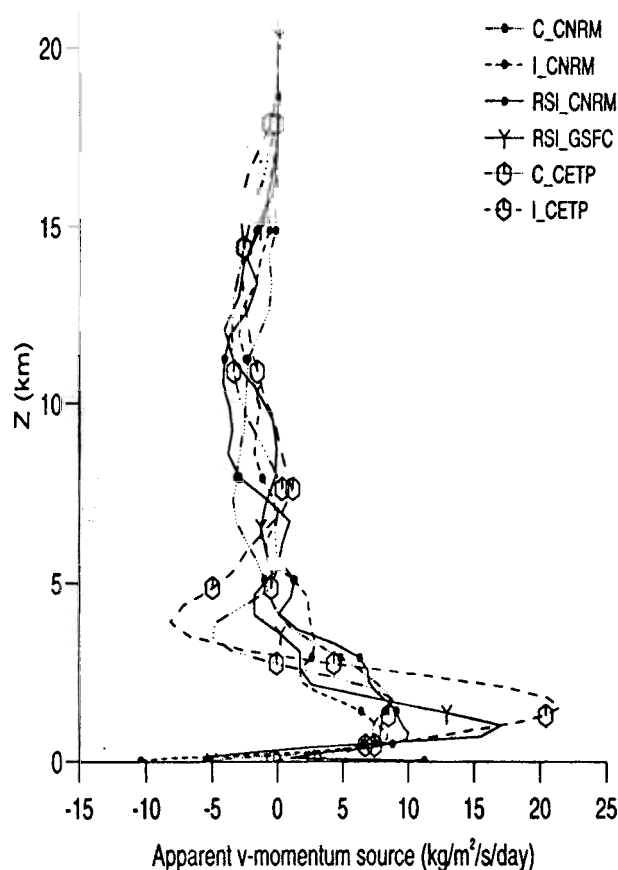


Figure 21. The vertical profiles of  $v$  (squall-line parallel) momentum source ( $\text{kg m}^{-2}\text{s}^{-1}\text{day}^{-1}$ ) averaged from 5 to 6 hours of the 3D cloud-resolving model (CRM) simulations (see Tables 1 and 4 for an explanation of the acronyms).

oscillatory behaviour, though the low levels are more coherent. This result is consistent with the previous discussion about the differences between the momentum profiles, and it supports a recommendation for using a 3D framework or, if not possible (e.g. for computational considerations), a 2D framework with a relaxation towards a mean horizontal wind (initial or observed). This latter approach has been used with success for the second case (see introduction) selected by the Precipitating Convective Cloud Systems Group of the GCSS (Krueger 1998). Although the use of a 2D model precludes the study of momentum transport, it keeps the wind profile closer to the observations, a key parameter in determining the convective organization. Examination of the profiles of momentum sources from the 3D simulations suggests that, on average, the effect of the convective system is to decrease the shear.

## 5 CONCLUSION

This GCSS intercomparison study has, for the first time, enabled the comparison of eight CRMs for the case of an oceanic tropical squall line observed during the TOGA-COARE experiment. Numerous papers have shown that the overall squall-line structure is determined from the cold pool and environmental wind shear (e.g. Thorpe *et al.* 1982; Redelsperger and Lafore 1988; Rotunno *et al.* 1988). This explains why, overall, both the 2D and 3D models performed well in simulating most of the main observed features of the squall line, in particular its structure and propagation. The goal of the present

work was also to perform a first quantitative intercomparison of quantities describing the convective intensity and the key features for parametrization in GCMs. Most of the models were also able to predict a similar rainfall and integrated water content evolutions and agreed quantitatively. The apparent heat and moisture sources also had a similar shape from model to model under some experimental configurations, though to a lesser extent. The 3D experiments with an ice-phase parametrization and with open lateral boundary conditions along the direction of system propagation showed good agreement for most parameters. Comparison of the 3D simulated fields with the ones derived from two different analyses of airborne Doppler radar data indicated that 3D models with open lateral boundary conditions along the direction of system propagation are able to simulate the proper dynamical structure.

Surface fluxes and radiative processes were found to have only a small impact on the experiments, slightly increasing the intensity of the convection and those quantities related to the rainfall. This conclusion is based on radiative processes invoked for a short period of time (7 hours). Also, with regard to surface fluxes, squall lines extract most of their energy from the ambient atmosphere thanks to their fast propagation. In contrast, some of the results were found to be sensitive to the microphysical scheme and to the framework dimensionality (2D versus 3D).

The line-averaged vertical motion taken from Doppler radar observations during the linear stage of the squall line displayed a double-peaked updraught structure. This feature was also simulated by the 3D CRMs. The second peak at around 10 km in height was obtained only when an ice-phase parametrization was used. The 2D simulations with an ice-phase parametrization also exhibited this structure, although  $x$  and  $z$  locations of these peaks differed. Snapshots indicate that the 2D experiments exhibited large temporal variability in their structures; this feature was also observed in the time series. The 2D simulations produced smaller values of maxima and minima of vertical velocity than the 3D ones (about half the magnitudes). For both 2D and 3D experiments the downdraught values were about half the updraught ones, a result also true for the mean values in the convective region. The use of periodic lateral boundary conditions along the direction of system propagation over a small domain was found to decrease the intensity of the system, giving a smaller stratiform region, lower vertical velocities and smaller water contents. In this case, full advection of hydrometeors ejected from the convective region was not allowed. Confirming this point, the 2D experiments using a large domain (1000 km) together with periodic lateral boundary conditions were well able to produce stratiform regions and showed a reasonable quantitative agreement for global parameters (such as the integrated water content and rainfall) with the 3D model results.

The impacts of the dimensionality, ice phase and lateral boundary conditions are summarized in Fig. 22. Ice-phase processes tend to increase both the vertical and the horizontal extent of the convective system significantly (Fig. 22(a)). The horizontal extent of the stratiform part depends, however, on the ice-phase parametrization; this is especially true in 2D. The squall line exhibits much less temporal variability in 3D than in 2D, with a less pronounced tilting. The 3D framework leads to the development of deeper convective cells and a larger stratiform region (Fig. 22(a)). In this respect, the ice-phase parametrization and the third dimension act in much the same way, although through different (by nature) processes. The model sensitivity to the lateral boundary conditions (Fig. 22(b)) is directly related to the impact of the interactions between the convective system and its large-scale environment. Different choices of lateral boundary conditions do not modify the basic convective features, such as the intensity of convective up- and downdraughts, the maximum vertical extent of the squall line,

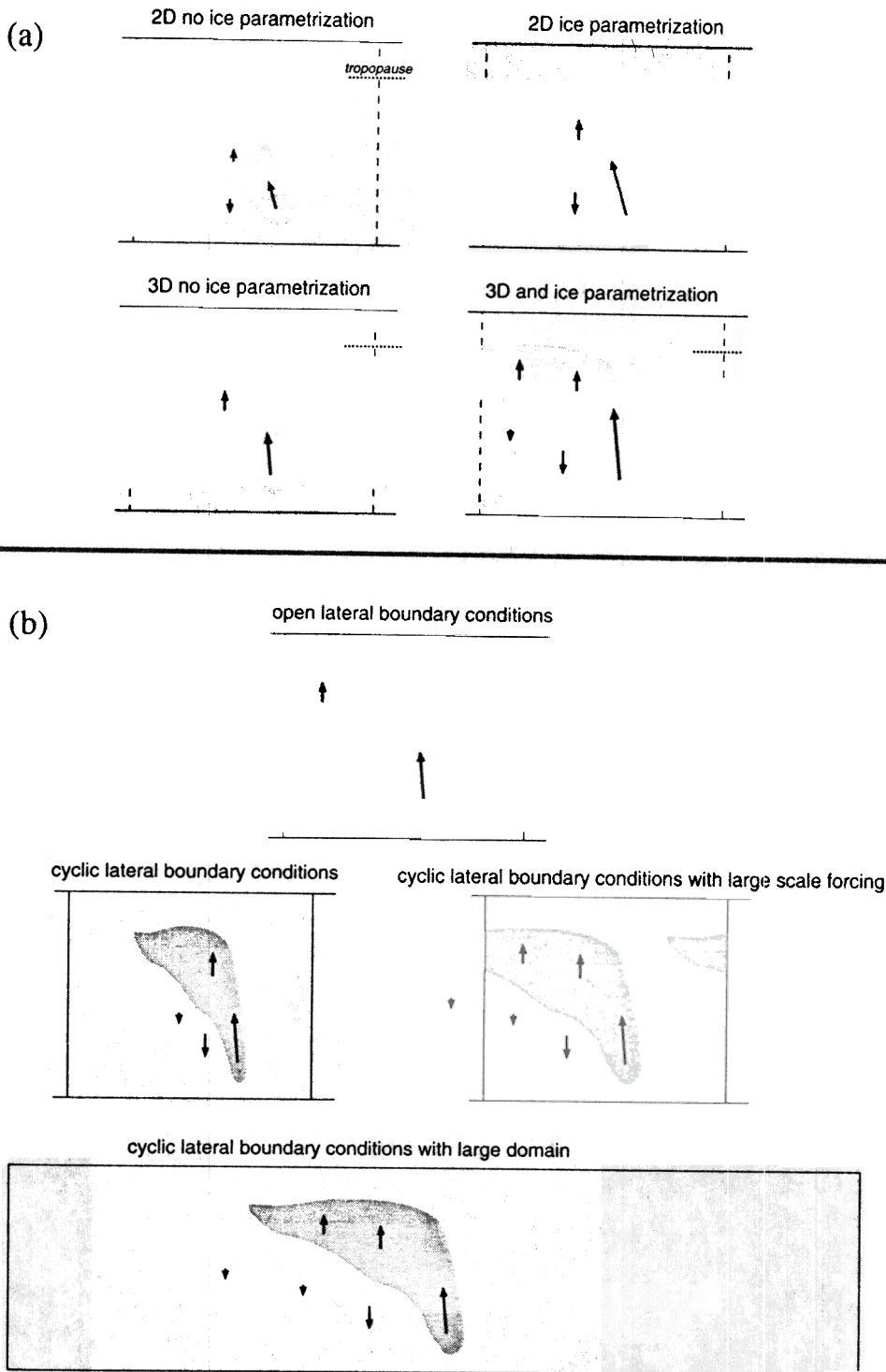


Figure 22. Schematic diagram showing the impact of (a) the dimensionality and ice-phase parametrization, and (b) the lateral boundary conditions (arrows indicate the mean vertical motion).

and parameters more strongly linked to the atmospheric mean state through the initial sounding. However, the horizontal extent of the stratiform region and the life cycle and time duration of the line critically depend on the mean vertical velocity experienced by the squall line and its close environment. With cyclic lateral boundary conditions, the mean vertical velocity is forced to zero and leads to a weaker squall line, with fewer convective cells and less stratiform activity than with open lateral boundary conditions.

Using a much larger domain than the width of the squall line itself (Fig. 22(b)) can to overcome this deficiency. When a mean large-scale ascent is applied to a domain with cyclic lateral boundary conditions (as in the second case of GCSS) the intensity of the convective system increases, although spurious effects can arise owing to the horizontal advection of hydrometeors.

Examination of the wind profile evolution and momentum sources from the 3D simulations suggests that, on average, the squall line has the main effect of decreasing the shear. This result is in contrast to the behaviour of African squall lines observed and simulated during the COPT81 experiment, where an increase in shear was found in some parts of the atmosphere. One possible reason, in agreement with the recent detailed analysis of Trier *et al.* (1998), is the relatively small linear portion of the present system, with different types of flow in the northern, southern and central parts of the squall line. The COPT81 case looked more like the central part of the present system. The 2D experiments were not able to capture the same evolution in wind. They predicted an increase of the jet and generally led to large vertical oscillations of the line-normal component of the wind. Theoretical explanations based on the continuity equation have been given. The treatment of lateral boundary conditions is also important for this matter. Thus, periodic lateral boundary conditions preclude any change in the vertical average of  $u$ -momentum in each column of the 2D models. This result suggests that in 2D it is better to relax the domain-average horizontal wind towards observed winds. This approach has been successfully followed for the other intercomparison case (Krueger 1998) and, whilst this precludes the study of momentum transport, the wind profile stays close to the observations, which is a key factor in determining the convective organization.

It is worth noting that this difficult and long exercise was found to be very useful by the participants in allowing them to check many parts of their codes and to find some errors. Clearly more confidence in the codes has been gained from this exercise. It is clear that this first intercomparison has to be considered only as a first step. Nevertheless, similarities and differences between 2D and 3D models have been identified on the basis of numerous experiments with the eight different models. Also, the results are a motivation to work to reduce the uncertainties coming from the microphysical parametrizations. As an example, discrepancies found with one of the 2D models when comparing with other models were reduced when the mean fall speed of cloud ice was increased. Though ice processes are generally thought to be important for time-scales  $\geq 1$  day, the present results show that they also need to be considered for time scales of few hours. This emphasises the importance of further study into the sensitivity of models to microphysical parametrizations for such case studies. In order to improve ice-phase parametrizations, the authors recommend the design of a field experiment fully dedicated to this fundamental issue. This should also include within the dataset in-situ observations of the upper-tropospheric cloud microphysical properties, measurements of which were unavailable during TOGA-COARE.

Finally, diagnostics issued from the intercomparison illustrate that datasets from CRMs validated against observations can be used to evaluate and develop cloud parametrizations used in large-scale models. Such an approach is presented in a companion paper (Bechtold *et al.* 1999).

#### ACKNOWLEDGEMENTS

We would like to express our gratitude to Dr M. Moncrieff who led the GCSS Precipitating Convective Clouds Working Group during the project. Enthusiastic support

from Prof K. Browning, the chairman of European Cloud-REsolving Modelling project (EUCREM) and GCSS, is gratefully acknowledged. Support from Prof S. Krueger was also appreciated. Discussions at the initial stage of the project with Drs S. Trier, M. A. LeMone and D. Jorgensen were helpful in setting up the initial conditions. Research at the CNRM/GAME and the Joint Centre for Mesoscale Meteorology (JCMM) were partly funded by the European Commission through the EUCREM project ENV4 CT95 0107. One of the authors of this paper (K. Nakamura) would like to thank the Center for Analysis and Prediction of Storms (University of Oklahoma), which was responsible for the development of the Advanced Regional Prediction System model. Runs performed at the Centre d'étude des Environnements Terrestre et Planétaires have benefitted from help of T. Biju, J. P. Lafore, J. P. Pinty, P. Jabouille and J. Stein. Two of the authors (W. K. Tao and S. Lang) were supported by the National Aeronautics and Space Administration (NASA) Tropical Rainfall Measuring Mission, and their computing resources were provided by the NASA Goddard Space Flight Center. The JCMM is supported by the UK Meteorological Office and the University of Reading.

## REFERENCES

- Bechtold, P., Redelsperger, J.-L., Beau, I., Blackburn, M., Brinkop, S., Grandpeix, J.-Y., Grant, A., Gregory, D., Guichard, F., Hoff, C. and Ioannidou, E. 2000 A GCSS model intercomparison for a tropical squall line observed during TOGA-COARE. II: Intercomparison of single-column models and a cloud-resolving model. *Q. J. R. Meteorol. Soc.*, **126**, 865–888
- Bretherton, C. S., MacVean, M. K., Bechtold, P., Chlond, A., Cotton, W. R., Cuxart, J., Cuijpers, H., Khairoutdinov, M., Kosovic, B., Lewellen, D., Moeng, C.-H., Siebesma, P., Stevens, B., Stevens, D. E., Sykes, I. and Wyatt, M. C. 1999 An intercomparison of radiatively driven entrainment and turbulence in a smoke cloud, as simulated by different numerical models. *Q. J. R. Meteorol. Soc.*, **125**, 391–424
- Caniaux, G., Redelsperger, J.-L. and Lafore, J.-P. 1994 A numerical study of the stratiform region of a fast-moving squall line. Part I. General description, and water and heat budgets. *J. Atmos. Sci.*, **51**, 2046–2074
- Caniaux, G., Lafore, J.-P. and Redelsperger, J.-L. 1995 A numerical study of the stratiform region of a fast-moving squall line. Part II: Relationship between mass, pressure and momentum fields. *J. Atmos. Sci.*, **52**, 331–352
- Chen, S. and Cotton, W. R. 1988 The sensitivity of a simulated extratropical mesoscale convective system to longwave radiation and ice-phase microphysics. *J. Atmos. Sci.*, **45**, 3897–3910
- Chong, M., Amayenc, P., Scialom, G. and Testud, J. 1987 A tropical squall line observed during the COPT81 experiment in West Africa. Part I: Kinematic structure inferred from dual-doppler radar data. *Mon. Weather Rev.*, **115**, 670–694.
- Donner, L. J., Seman, C.J. and Hemler, R.S. 1999 Three-dimensional cloud-system modeling of GATE convection. *J. Atmos. Sci.*, **56**, 1885–1912
- Fovell R. G. and Ogura, Y. 1988 Numerical simulation of a midlatitude squall line in two dimensions. *J. Atmos. Sci.*, **45**, 3846–3879
- Gates, W. L. 1992 AMIP: The atmospheric model intercomparison project. *Bull. Amer. Meteorol. Soc.*, **73**, 1962–1970
- Held I. M., Hemler, R. S. and Ramaswamy, V. 1993 Radiative-convective equilibrium with explicit two-dimensional moist convection. *J. Atmos. Sci.*, **50**, 3911–3927
- Houze, R. A. 1977 Structure and dynamics of a tropical squall line system observed during GATE. *Mon. Weather Rev.*, **105**, 1540–1567
- Ikawa, M. and Saito, K. 1991 'Description of a nonhydrostatic model developed at the Forecast Research Department of the MRI'. MRI Tech. Rep. **28**, (available from the Meteorology Research Institute, Tsukuba, Japan)
- Jorgensen, D. P., LeMone, M. A. and Trier, S. B. 1997 Structure and evolution of the 22 February 1993 TOGA-COARE squall line: Observations of precipitation, circulation, and surface energy fluxes. *J. Atmos. Sci.*, **54**, 1961–1985

- Krueger, S. K. 1998 'A GCSS intercomparison of cloud-resolving models based on TOGA-COARE observations'. Pp113-127 in Proceedings of the workshop in 'New insights and approaches to convective parametrization', European Centre for Medium-Range Weather Forecasts, Reading, UK
- Lafore, J.-P., Redelsperger, J.-L. and Jaubert, G. 1988 Comparison between a three-dimensional simulation and Doppler radar data of a tropical squall line: Transports of mass, momentum heat and moisture. *J. Atmos. Sci.*, **45**, 3483-3500
- Lafore, J.-P., Stein, J., Asencio, N., Bougeault, P., Ducrocq, V., Duron, J., Fisher, C., Hireil, Ph., Mascart, P., Pinty, J. P., Redelsperger, J.-L., Richard, E. and Vil-Guerau de Arellano, J. 1998 The Meso-NH atmospheric simulation system. Part I: Adiabatic formulation and control simulations, *Ann. Geophys.*, **16**, 90-109
- LeMone, M. A., Jorgensen, D. P. and Smull, B. F. 1994 'The impact of two convective systems of sea-surface stresses in COARE'. Pp. 40-44 in Preprints of the 6th conference on mesoscale processes, American Meteorological Society, Portland, USA
- LeMone, M. A., Zipser, E. J. and Trier, S. B. 1998 The role of environmental shear and CAPE in determining the structure and evolution of mesoscale convective systems during TOGA-COARE, *J. Atmos. Sci.*, **55**, 3493-3564
- Lin, Y. L., Farley, R. D. and Orville, H. D. 1983 Bulk parameterization of the snow field in a cloud model. *J. Climate Appl. Meteorol.*, **22**, 1065-1092
- Liu, C., Moncrieff, M. W. and Zipser, E. J. 1997 Dynamical influence of microphysics in tropical squall lines: A numerical study. *Mon. Weather Rev.*, **125**, 2193-2210
- Moeng, C.-H., Cotton, W. R., Bretherton, C. S., Chlond, A., Khairoutdinov, M., Krueger, S. K., Lewellen, W. S., MacVean, M. K., Pasquier, J. R., Rand, H. A., Siebesma, A. P., Sykes, R. I. and Stevens, B. 1996 Simulation of a stratocumulus-topped PBL: Intercomparison among different numerical codes. *Bull. Amer. Meteorol. Soc.*, **77**, 261-278
- Moncrieff M. W., Gregory, D., Krueger, S. K., Redelsperger, J.-L. and Tao, W. K. 1997 GEWEX Cloud System Study (GCSS) Working Group 4: Precipitating convective cloud systems. *Bull. Amer. Meteorol. Soc.*, **78**, 831-845
- Montmerle, Th. and Lemaitre, Y. 1998 Three-dimensional variational data analysis to retrieve thermodynamical fields from various nested wind measurements. *J. Atmos. Ocean. Technol.*, **7**, 640-665
- Nicholls, M. E. 1987 A comparison of the results of a two-dimensional numerical simulation of a tropical squall line with observations. *Mon. Weather Rev.*, **115**, 3055-3077
- Pinty, J. P. and Jabouille, P. 1998 'A mixed-phased cloud parameterization for use in a mesoscale non-hydrostatic model: simulations of a squall line and of orographic precipitation'. In the Proceedings of the cloud physics conference, American Meteorological Society, Boston, USA
- Redelsperger, J.-L. and Sommeria, G. 1986 Three-dimensional simulation of a convective storm : sensitivity studies on subgrid parameterization and spatial resolution. *J. Atmos. Sci.*, **43**, 2619-2635.
- Redelsperger, J.-L. and Lafore, J.-P. 1988 Three-dimensional simulation of a tropical squall-line: Convective organization and thermodynamic vertical transports. *J. Atmos. Sci.*, **45**, 1334-1356
- Redelsperger J.-L., Gregory, D., Krueger, S. K., Moncrieff, M. W. and Tao, W. K. 1996 'GEWEX Cloud System Study (GCSS) on precipitating convective cloud systems model intercomparisons. CASE 1: Tropical oceanic convection of TOGA-COARE'. Unpublished (available from J. -L. Redelsperger, CNRM/GAME, 42 Avenue Coriolis, 31057 Toulouse, France, or from <http://www.cnrm.meteo.fr/gcss/>)
- Rickenbach, T. M. and Rutledge, S. A. 1998 Convection in TOGA-COARE: Horizontal scale, morphology, and rainfall production. *J. Atmos. Sci.*, **55**, 2715-2729
- Rotunno, R., Klemp, J. B. and Weisman, M. L. 1988 A theory for strong, long-lived squall lines. *J. Atmos. Sci.*, **45**, 463-485

- Rutledge, S. A., Houze, R. A. Jr., Biggerstaff, M. I. and Matejka, T. 1988 The Oklahoma–Kansas mesoscale convective system of 10–11 June 1985: Precipitation structure and single-Doppler radar analysis. *Mon. Weather Rev.*, **116**, 1409–1430
- Saito, K. and Kato, T. 1996 On the modification of the MRI nonhydrostatic nesting model. *Tenki*, **43**, 369–382
- Short, A. D., Kucera, P. A., Ferrier, B. S., Gerlach, J. C., Rutledge, S. A. and Thiele, O. W. 1997 Shipboard radar rainfall patterns within the TOGA COARE IFA. *Bull. Amer. Meteorol. Soc.*, **78**, 2817–2836
- Shutts, G.J. and Gray, M. 1994 A numerical modelling study of the geostrophic adjustment process following deep convection. *Q. J. R. Meteorol. Soc.*, **120**, 1145–1178
- Slingo J. M., Sperber, K. R., Boyle, J. S., Ceron, J. P., Dix, M., Dugas, B., Ebisuzaki, W., Fyfe, J., Gregory, D., Gueremy, J. F., Hack, J., Harzallah, A., Inness, P., Kitoh, A., Lau, W. K., McAvaney, B., Madden, R., Mathews, A., Palmer, T. N., Park, C.-K., Randall, D. and Renno, N. 1996 Intraseasonal oscillations in 15 atmospheric general circulation models: results from an AMIP diagnostic subproject. *Clim. Dynamics*, **12**, 325–357
- Swann, H. A. 1996 'The development and validation of a microphysics scheme for cloud-resolving model studies of deep convection'. Ph.D. thesis, University of Reading, UK
- Tao, W.-K. and Simpson, J. 1989 Modeling study of a tropical squall type convective line. *J. Atmos. Sci.*, **46**, 177–202
- The Goddard cumulus ensemble model. Part I: Model description. *Terr. Atmos. Ocean. Sci.*, **4**, 35–72
- Tao, W.-K., Simpson, J., Sui, C.-H., Ferrier, B., Lang, S. Scala, J., Chou, M.-D. and Pickering, K. 1993 Heating, moisture, and water budgets of tropical and midlatitude squall lines: Comparisons and sensitivity of longwave radiation. *J. Atmos. Sci.*, **50**, 673–690
- Tao, W.-K., Simpson, J. and Ferrier, B. 1997 'Simulations of mesoscale convective systems'. Pp. 77–112 in the Proceedings of the ECMWF workshop on new insights and approaches to convective parametrization, European Centre for Medium-Range Weather Forecasts, Shinfield Park, Reading, UK
- Thorpe, A. J., Miller M. J. and Moncrieff, M. W. 1982 Two-dimensional convection in non-constant shear: A model of mid-latitude squall lines. *Q. J. R. Meteorol. Soc.*, **108**, 739–762
- Trier, S. B., Skamarock, W. C., LeMone, M. A., Parsons, D. B. and Jorgensen, D. P. 1996 Structure and evolution of the 22 February 1993 TOGA–COARE squall line: Numerical simulations. *J. Atmos. Sci.*, **53**, 2861–2886
- Trier, S. B., Skamarock, W. C. and LeMone, M. A. 1997 Structure and evolution of the 22 February 1993 TOGA–COARE squall line: Organization mechanisms inferred from numerical simulation. *J. Atmos. Sci.*, **54**, 386–407
- Trier, S. B., LeMone, M. A and Skamarock, W. C. 1998 Effect of three-dimensional structure on the stormwide horizontal accelerations and momentum budget of a simulated squall line. *Mon. Weather Rev.*, **126**, 2580–2598
- Wang, Y., Tao, W.-K. and Simpson, J. 1996 The impact of a surface layer on TOGA–COARE cloud system development. *Mon. Weather Rev.*, **124**, 2753–2763
- Xue, M., Droegeheimer, K. K., Wong, V., Shapiro, A. and Brewster, K. 1995 'ARPS Version 4.0 User's Guide'. Unpublished (available from the Center for Analysis and Prediction of Storms, University of Oklahoma, 100 E. Boyd St., Norman OK 73019, USA)
- Yoshizaki, M. 1986 Numerical simulations of tropical squall line clusters: Two-dimensional model. *J. Meteorol. Soc. Japan*, **64**, 469–491
- Zipser, E. J. 1977 Mesoscale and convective scale downdrafts as distinct components of squall-line circulation. *Mon. Weather Rev.*, **105**, 1568–1589